Supplementary Information

Composition-invariant strain engineering of metal sulfides for efficient hydrogen evolution

Hongfang Du,[a,b] Ke Wang,[b] Song He,[b] Boxin Li,[b] and Wei Ai[b,*]

[a] Strait Laboratory of Flexible Electronics (SLoFE), Fujian Key Laboratory of Flexible Electronics, Strait Institute of Flexible Electronics (SIFE Future Technologies), Fujian Normal University, Fuzhou 350117, China

[b] State Key Laboratory of Flexible Electronics & Institute of Flexible Electronics, Northwestern Polytechnical University, Xi'an 710072, China

* Corresponding Author

E-mail: iamwai@nwpu.edu.cn (W. Ai)

1 Experimental Section

1.1 Chemicals and materials

$CrCl_3·6H_2O$ (99%), $MnCl_2·4H_2O$ (99%), $FeCl_2·4H_2O$ (98%), $CoCl_2·6H_2O$ (99%), $CuCl_2$ (98%), $ZnCl_2$ (99.99%), $Na_2MoO_4·2H_2O$ (99%), $RuCl_3·3H_2O$ (98%), $PdCl_2$ (99%), $CdCl_2·5H_2O$ (98%), $InCl_3·4H_2O$ (99.9%), $SnCl_2$ (99%), $ReCl_3$ (99.99%), and $PbCl_2$ (99%) were purchased from Adamas-beta. Nafion solution (5 wt% in lower aliphatic alcohols) was obtained from Sigma-Aldrich. NH_4VO_3 (99%), $Bi(NO_3)_3·5H_2O$ (99%), $NiCl_2$ (98%), $RhCl_3$ (98%), $OsCl_3·3H_2O$ (99%), $AgNO_3$ (99%), $H_2PtCl_6·6H_2O$ (99.9%), KOH (90%), and KSCN (98.5%) were supplied by Aladdin. rGO was provided by the Institute of Coal Chemistry, Chinese Academy of Sciences. All chemicals were used as received without further purification.

1.2 Synthesis of s-TMSs/NSG

Typically, 150 mg of reduced graphene oxide (rGO), 0.1 mmol of $RuCl_3·3H_2O$ (26.1 mg), and 60 g of KSCN were thoroughly ground in an agate mortar and transferred to a beaker. The mixture was heated at 450 °C for 2 h in an integrated programmable atmosphere box furnace to implement the molten-salt reaction. During the heating process, KSCN melted and reacted with rGO and Ru precursors to produce RuS_2/NSG composites. After the molten-salt reaction, the system was cooled at different rates to introduce distinct tensile strains. An ultra-slow cooling at 1 °C min^{-1} yielded unstrained RuS_2/NSG-0.0%. Faster quenching at 20, 40, 60, and 80 °C min^{-1} produced RuS_2/NSG-0.7%, RuS_2/NSG-2.8%, RuS_2/NSG-5.0%, and RuS_2/NSG-6.8%, respectively. Cooling rates ranging from 1 to 80 C·min^{-1} were precisely and reproducibly regulated using an integrated programmable furnace equipped with a high-precision proportional–integral–derivative (PID) feedback system, combined with adjustable Ar gas flow and forced convection modules. The ultra-slow cooling rate of 1 C·min^{-1} was achieved via programmed linear temperature decline with a fully closed furnace cavity and all auxiliary cooling devices closed, relying on slow radiation and natural heat dissipation to eliminate thermal gradient. The cooling rate of 20 °C min^{-1} was realized by natural cooling under a static Ar atmosphere. The medium cooling rates of 40 and 60 C·min^{-1} were accurately controlled by adjusting the power and Ar flow rate of the forced Ar convection module to enhance uniform convective heat transfer. The maximum cooling rate of 80 C·min^{-1} was achieved via rapid quenching using high-flow, low-temperature Ar gas, enabling efficient extraction of heat from both the surface and bulk of the molten salt system. The resulting

products were washed several times with deionized water and ethanol to remove residual salts, followed by drying at room temperature. Other strained transition metal sulfide/NSG (s-TMSs/NSG) composites were synthesized under the same conditions (450 °C, 2 h, quenching rate of 40 °C min^{-1}) by replacing Ru salts with corresponding metal precursors. Strain-relaxed RuS_2/NSG-2.8*% was obtained by annealing RuS_2/NSG-2.8% in Ar at 400 °C for 2 h, followed by slow cooling at 1 °C min^{-1}.

1.3 Characterization

XRD was conducted on a Bruker D8 ADVANCE diffractometer with Cu Kα radiation (λ = 1.5406 Å). SEM images were obtained on a FEI Verios G4 microscope. TEM, double Cs-corrected TEM, HAADF-STEM, and EDS analyses were performed on a FEI Themis Z microscope. XPS and UPS were carried out using a Thermo Fisher ESCALAB 250Xi system. XAFS measurements at the Ru K-edge were performed at the Taiwan Synchrotron Radiation Facility. The data were processed using Athena and Artemis in the Demeter software suite. The EPR analysis was performed with a BRUKER EMX plus-10/12 electron spin spectrometer at room temperature. The pH of the electrolytes was measured with a METTLER TOLEDO pH meter (FP20 Five Easy Plus).

1.4 Electrochemical measurements

Electrocatalytic tests were conducted on an Autolab PGSTAT 302N workstation in a conventional three-electrode setup. A saturated calomel electrode (SCE, equipped with a salt bridge) was used at the reference electrode, and its potential was calibrated against a commercial standard hydrogen electrode (SHE) for accuracy (Fig. S16). A graphite rod and a piece of nickel foam (sealed with molten wax) served as the counter and working electrodes, respectively. Solutions of 0.5 M H_2SO_4 in deionized water (pH = 0.4), 1.0 M KOH in deionized water (pH = 13.81), and 1.0 M KOH in seawater (pH = 13.74) were applied as electrolytes for electrochemical measurements. The seawater was collected from the Qiongzhou Strait (northern Hainan Province, China). Catalyst inks were prepared by dispersing 10.0 mg of catalyst in 1.0 mL of ethanol containing 25 μL of Nafion solution under ultrasonication for 15 min. The ink was drop-cast onto nickel foam with a loading of 1.0 mg cm^{-2}. Linear sweep voltammetry curves were recorded at 5 mV s^{-1}. Stability evaluated by CV was conducted in the range −0.1 to 0 V at 100 mV s^{-1}. Electrochemical impedance spectroscopy (EIS) was measured in a frequency range of 0.1 – 100000 Hz with an AC amplitude of 5 mV and an overpotential of 100 mV. All potentials were converted to the reversible hydrogen electrode

(RHE) scale using: $E_{RHE} = E_{SCE} + 0.242 + 0.059pH$. All electrochemical data were corrected for Ohmic losses (iR compensation).

1.5 AEMWE testing

The membrane electrode assembly (MEA) employed a 60-μm-thick anion-exchange membrane (QZ-AEM, Changzhou Aemhy Hydrogen Energy Technology Co., LTD). The HER cathode catalyst layer was fabricated by ultrasonic spraying of catalyst ink containing 60 mg catalyst powder, 0.375 g of 5 wt% ionomer solution in ethanol, 0.750 g deionized water, and 3 g isopropanol homogenized onto carbon paper (TGP-H-060) to achieve a loading of ~2 mg cm^{-2}. The anode featured self-supported NiFe-LDH on nickel foam. Electrolyzer tests were performed with 1.0 M KOH in seawater electrolyte at 60 °C. The current density was normalized to the geometric electrode area (1 cm^2) without iR compensation.

1.6 Theoretical calculations

First-principles calculations were performed using the Vienna ab initio simulation package. The NSG substrate was modeled as a single-layer graphene 8 × 4 × 1 supercell (64 C atoms, ICSD No. 31170), where two C atoms were replaced by one N and one S atom, or four C atoms were replaced by two N and two S atoms. RuS_2 was modeled using a Ru-terminated RuS_2 (200) slab comprising three layers (ICSD No. 68472; a = b = c = 5.61 Å, α = β = γ = 90°). The slab (36 Ru and 60 S atoms) was stacked on NSG to form RuS_2/NSG-0.0%. Strained models were generated by varying the in-plane lattice constants of RuS_2. The generalized gradient approximation with the Perdew-Burke-Ernzerhof functional described exchange-correlation effects. The projector augmented-wave method was used with a plane-wave cutoff energy of 400 eV. Gaussian smearing (0.05 eV width) was applied, and electronic convergence was set to 10^{-4} eV. Geometry optimization proceeded until atomic forces were below 0.05 eV $Å^{-1}$. Brillouin-zone integrations used a 2 × 2 × 1 Monkhorst-Pack k-point mesh. Reaction free energies were computed using the computational hydrogen electrode model (*J. Phys. Chem. B* **2004**, *108*, 17886): $\Delta G = \Delta E + \Delta E_{ZPE} - T\Delta S$, where ΔE is the total energy change, ΔE_{ZPE} is the zero-point energy correction, ΔS is the entropy change, and T = 300 K.

2 Supporting Figures

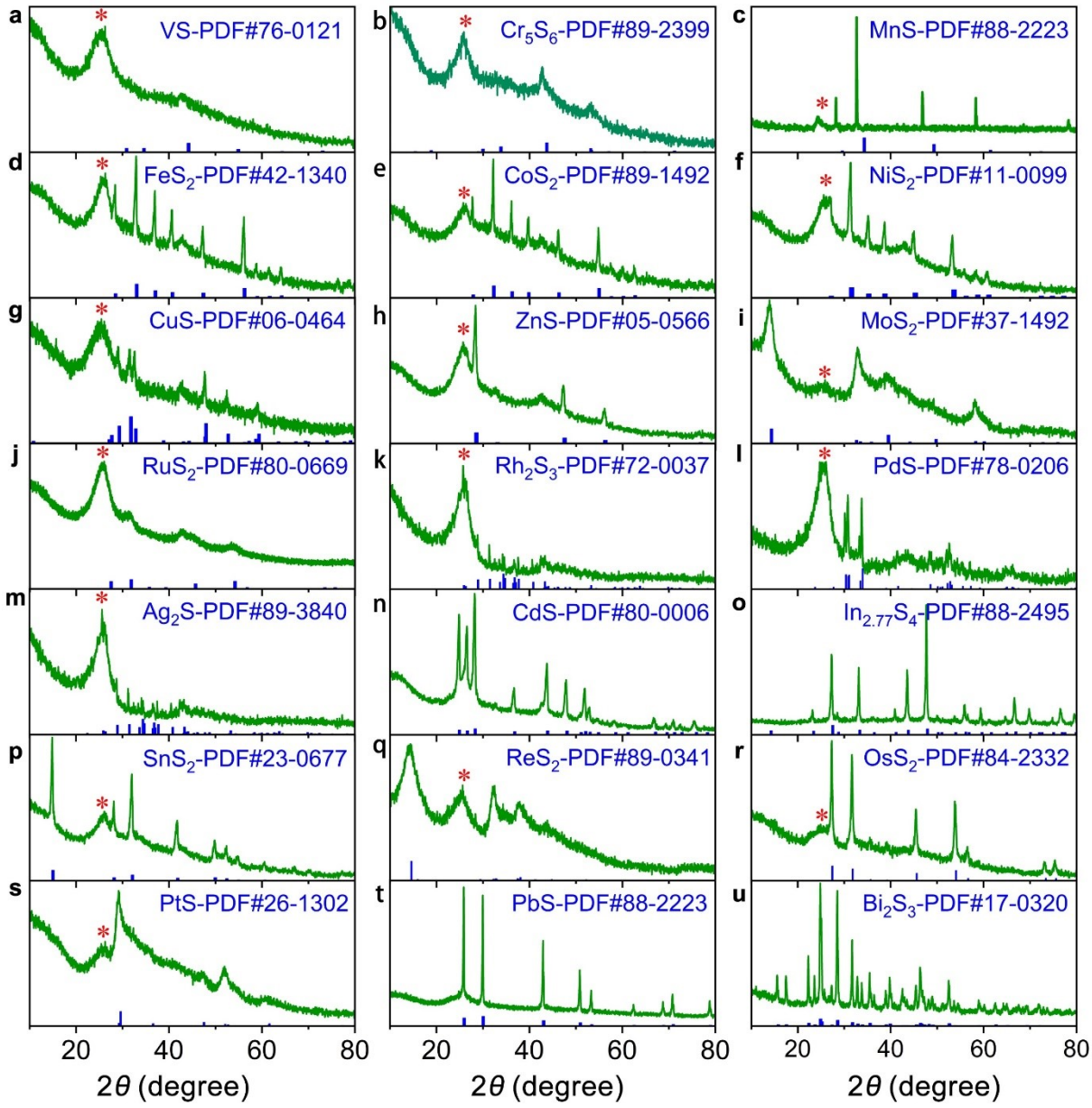

Fig. S1. XRD patterns of (a) s-VS/NSG, (b) s-Cr_5S_6/NSG, (c) s-MnS/NSG, (d) s-FeS_2/NSG, (e) s-CoS_2/NSG, (f) s-NiS_2/NSG, (g) s-CuS/NSG, (h) s-ZnS/NSG, (i) s-MoS_2/NSG, (j) s-RuS_2/NSG, (k) s-Rh_2S_3/NSG, (l) s-PdS/NSG, (m) s-Ag_2S/NSG, (n) s-CdS/NSG, (o) s-$In_{2.77}S_4$/NSG, (p) s-SnS_2/NSG, (q) s-ReS_2/NSG, (r) s-OsS_2/NSG, (s) s-PtS/NSG, (t) s-PbS/NSG, and (u) s-Bi_2S_3/NSG**.** The peak marked by the red asterisk stems from NSG.

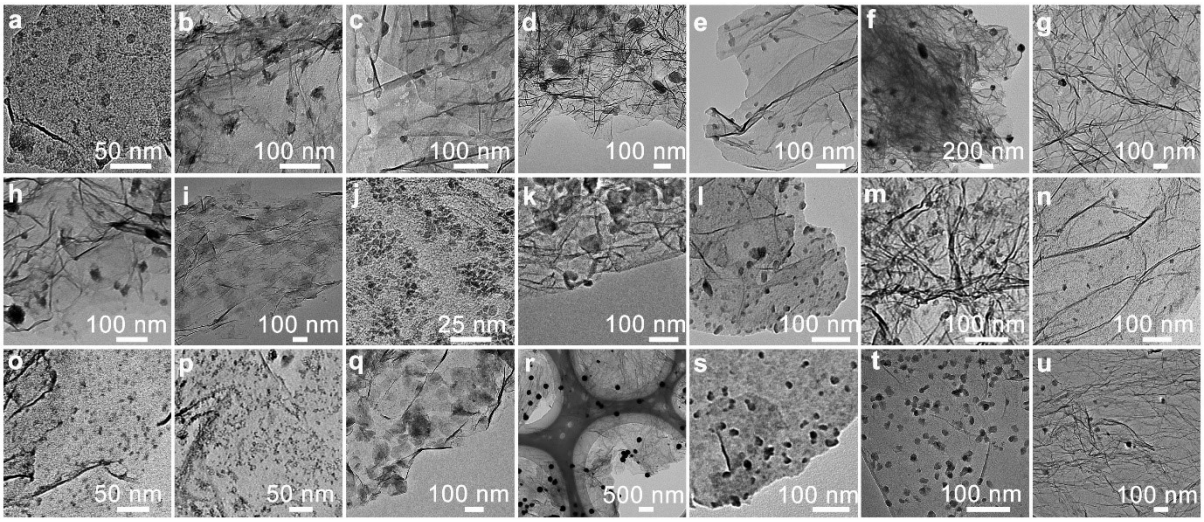

Fig. S2. TEM images of (a) s-VS/NSG, (b) s-Cr_5S_6/NSG, (c) s-MnS/NSG, (d) s-FeS_2/NSG, (e) s-CoS_2/NSG, (f) s-NiS_2/NSG, (g) s-CuS/NSG, (h) s-ZnS/NSG, (i) s-MoS_2/NSG, (j) s-RuS_2/NSG, (k) s-Rh_2S_3/NSG, (l) s-PdS/NSG, (m) s-Ag_2S/NSG, (n) s-CdS/NSG, (o) s-$In_{2.77}S_4$/NSG, (p) s-SnS_2/NSG, (q) s-ReS_2/NSG, (r) s-OsS_2/NSG, (s) s-PtS/NSG, (t) s-PbS/NSG, and (u) s-Bi_2S_3/NSG**.**

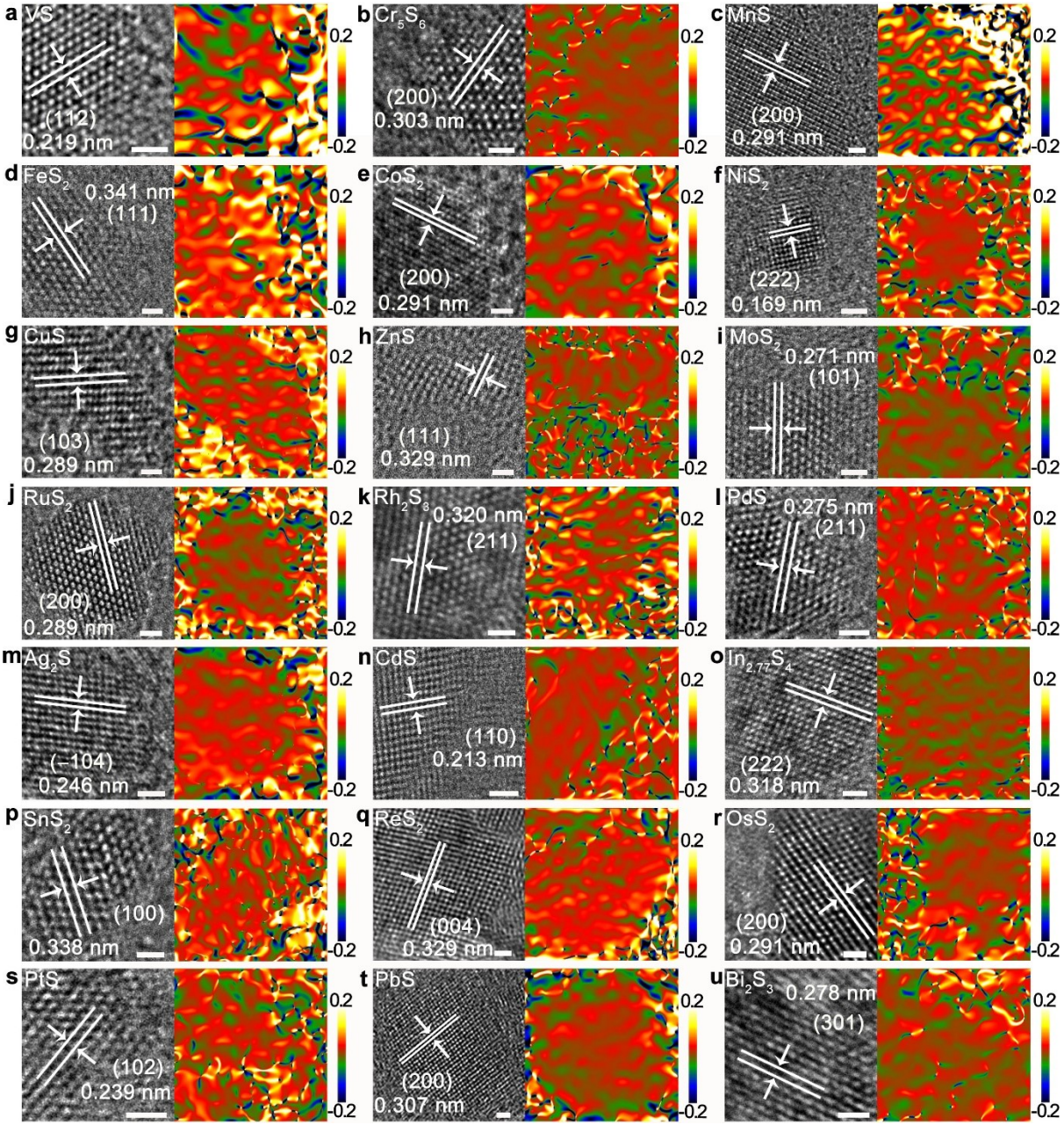

Fig. S3. Aberration-corrected HRTEM images and the corresponding GPA strain tensor maps in ε_{yy} direction of (a) s-VS/NSG, (b) s-Cr_5S_6/NSG, (c) s-MnS/NSG, (d) s-FeS_2/NSG, (e) s-CoS_2/NSG, (f) s-NiS_2/NSG, (g) s-CuS/NSG, (h) s-ZnS/NSG, (i) s-MoS_2/NSG, (j) s-RuS_2/NSG, (k) s-Rh_2S_3/NSG, (l) s-PdS/NSG, (m) s-Ag_2S/NSG, (n) s-CdS/NSG, (o) s-$In_{2.77}S_4$/NSG, (p) s-SnS_2/NSG, (q) s-ReS_2/NSG, (r) s-OsS_2/NSG, (s) s-PtS/NSG, (t) s-PbS/NSG, and (u) s-Bi_2S_3/NSG**.** The scale bar for all the images is 1 nm.

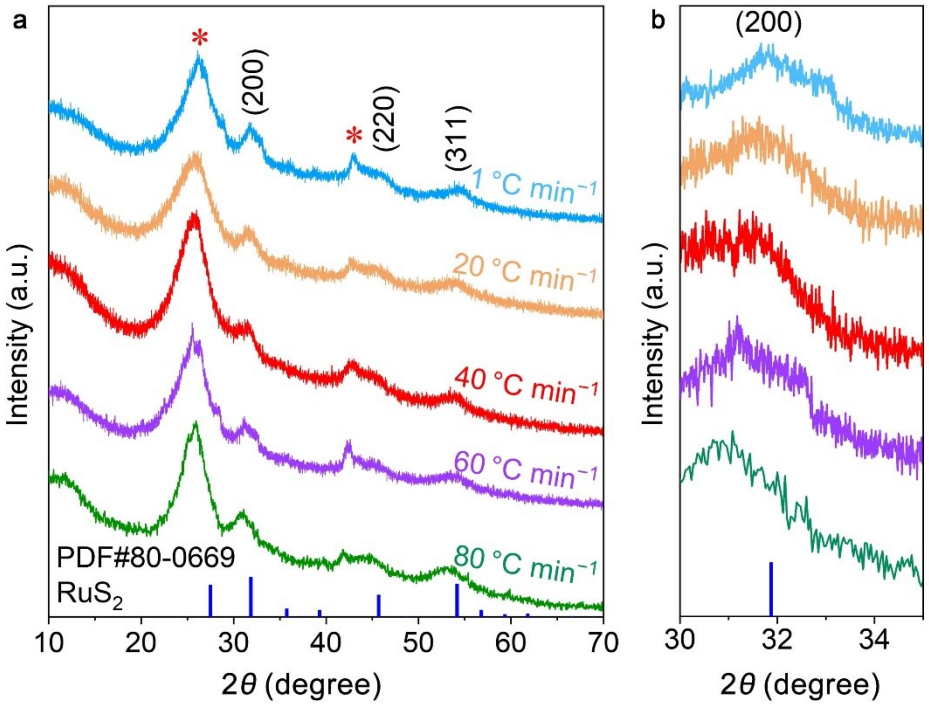

Fig. S4. (a) XRD patterns of s-RuS_2/NSG composites synthesized at various quenching rates. (b) Enlarged XRD patterns in the selected 2θ range between 30° and 35°.The peaks marked by the red asterisks are assignable to NSG.

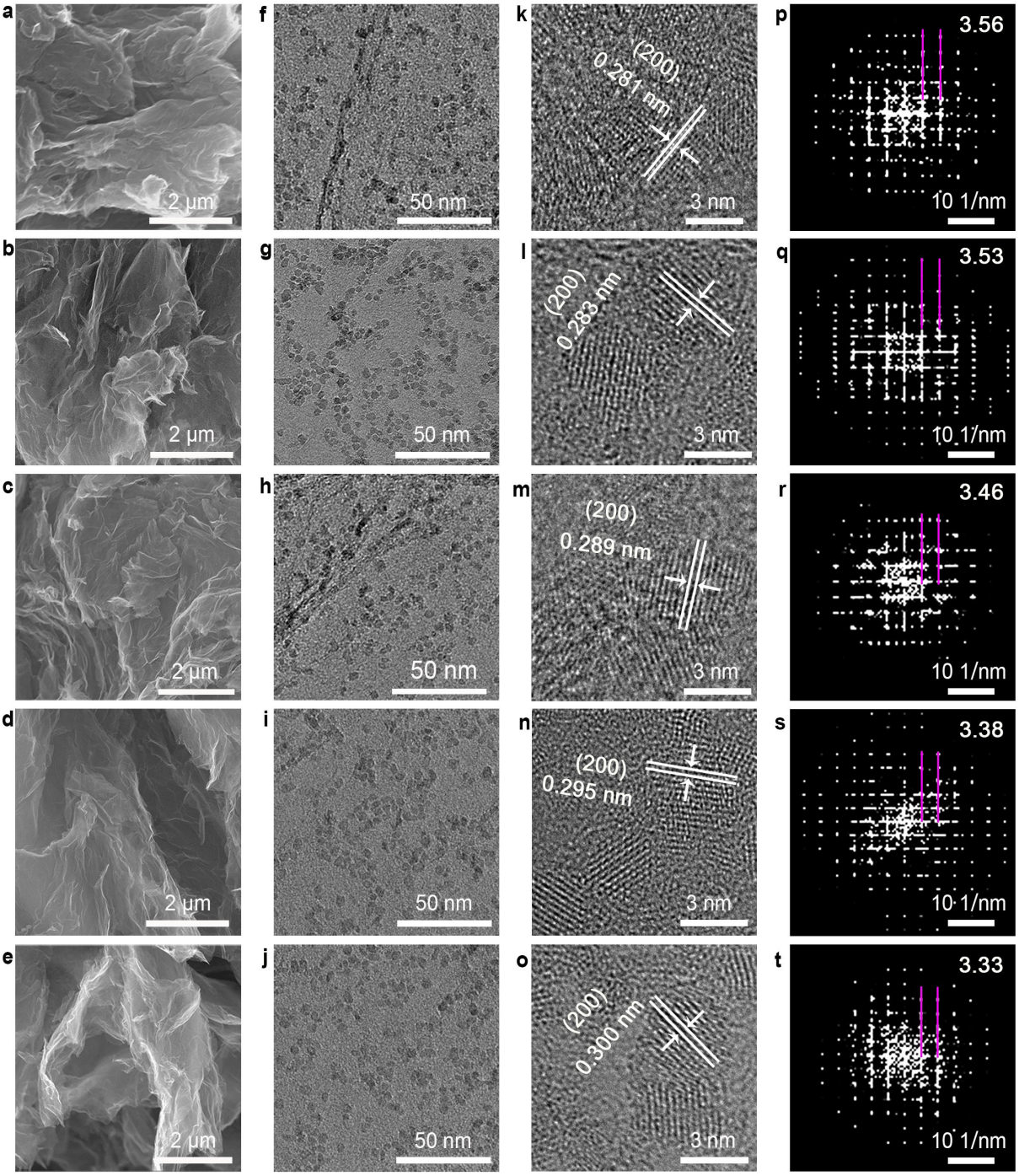

Fig. S5. (a-e) SEM images, (f-j) TEM images, (k-o) HRTEM images, and (p-t) FFT patterns of s-RuS_2/NSG composites synthesized at a quenching rate of (a, f, k, p) 1 °C min^{-1}, (b, g, l, q) 20 °C min^{-1}, (c, h, m, r) 40 °C min^{-1}, (d, i, n, s) 60 °C min^{-1}, and (e, j, o, t) 80 °C min^{-1}.

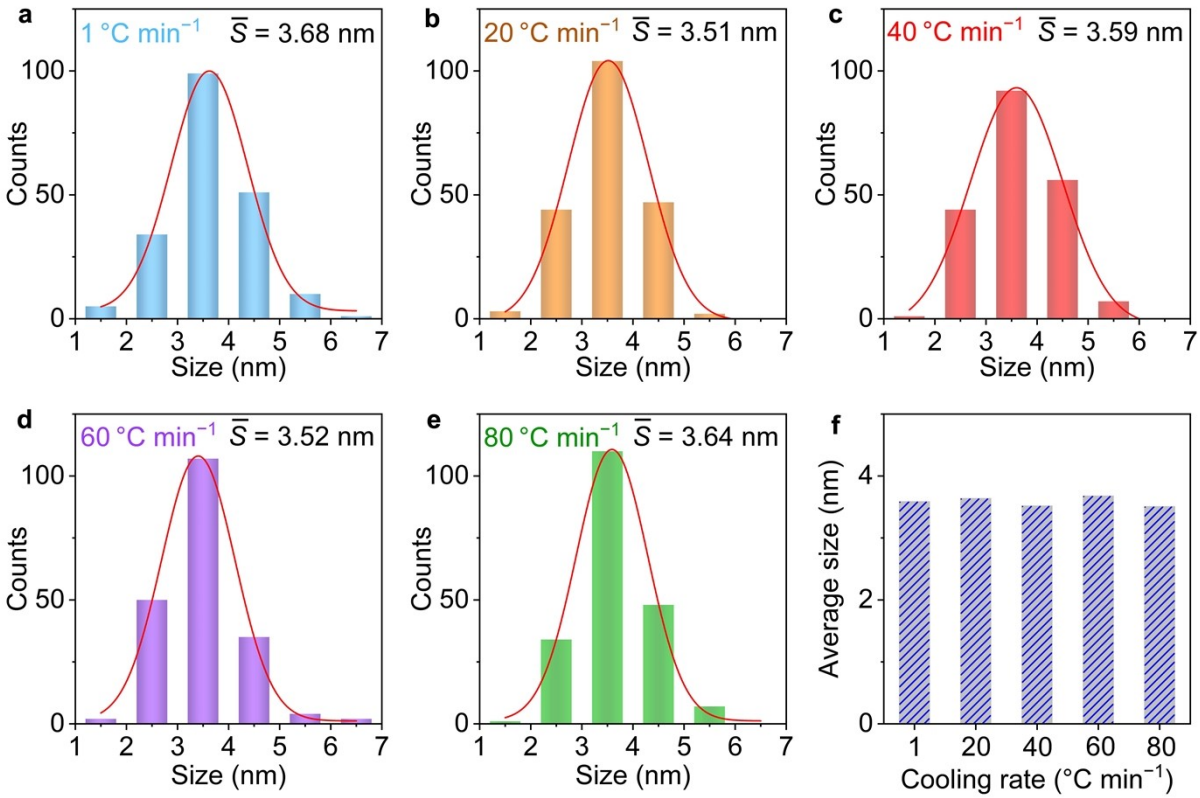

Fig. S6. Particle size distribution histograms of RuS_2 nanoparticles in s-RuS_2/NSG composites synthesized at quenching rates of (a) 1 °C min^{-1}, (b) 20 °C min^{-1}, (c) 40 °C min^{-1}, (d) 60 °C min^{-1}, and (e) 80 °C min^{-1}. (f) Average size of the RuS_2 nanoparticles in s-RuS_2/NSG composites.

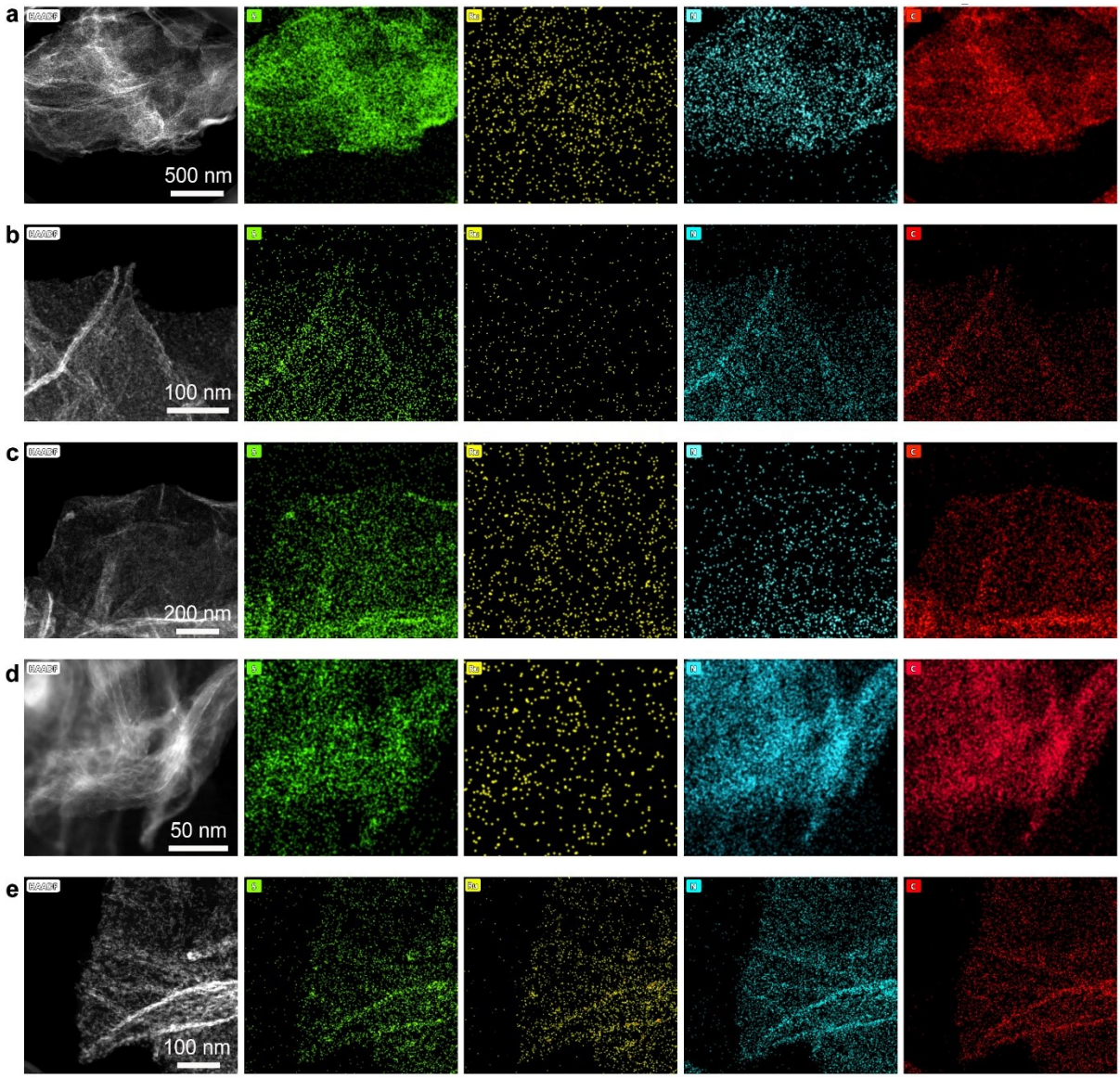

Fig. S7. STEM and corresponding EDS mapping images of s-RuS_2/NSG composites synthesized at quenching rates of (a) 1 ℃ min^{-1}, (b) 20 ℃ min^{-1}, (c) 40 ℃ min^{-1}, (d) 60 ℃ min^{-1}, and (e) 80 ℃ min^{-1}.

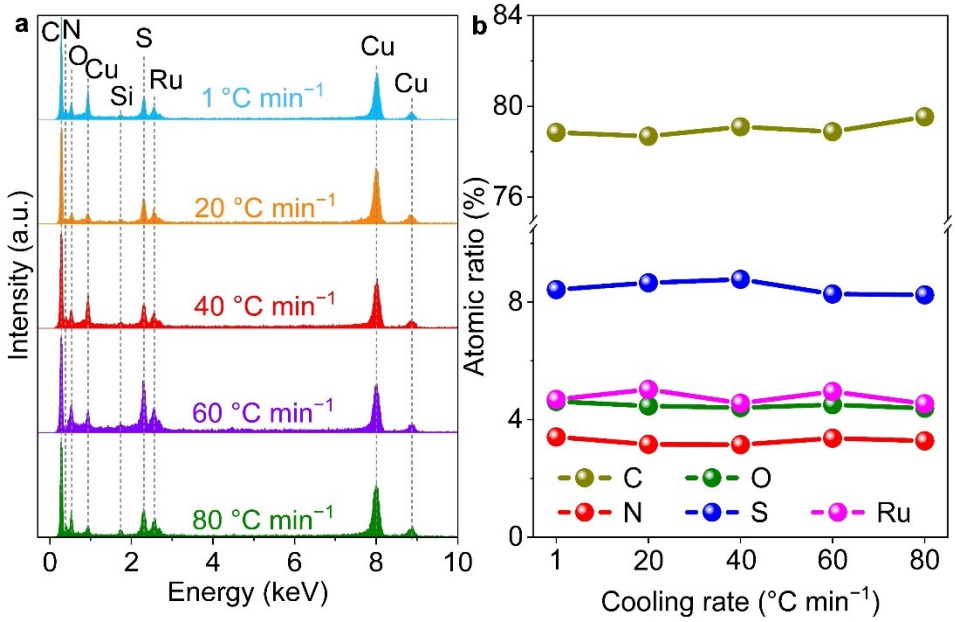

Fig. S8. (a) EDS spectra and (b) corresponding atomic ratios of s-RuS_2/NSG composites synthesized at various quenching rates.

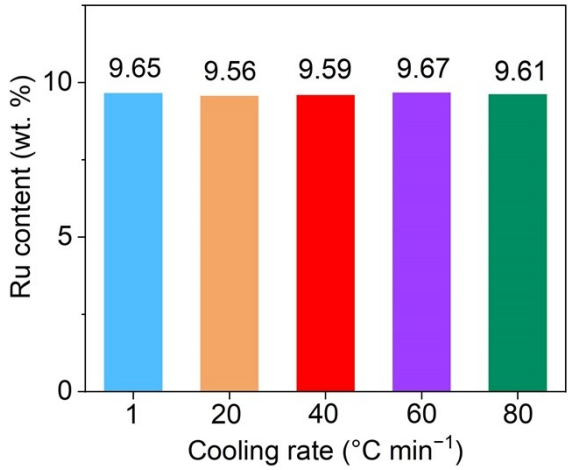

Fig. S9. ICP-OES analyses of Ru content in the s-RuS_2/NSG composites synthesized at different quenching rates.

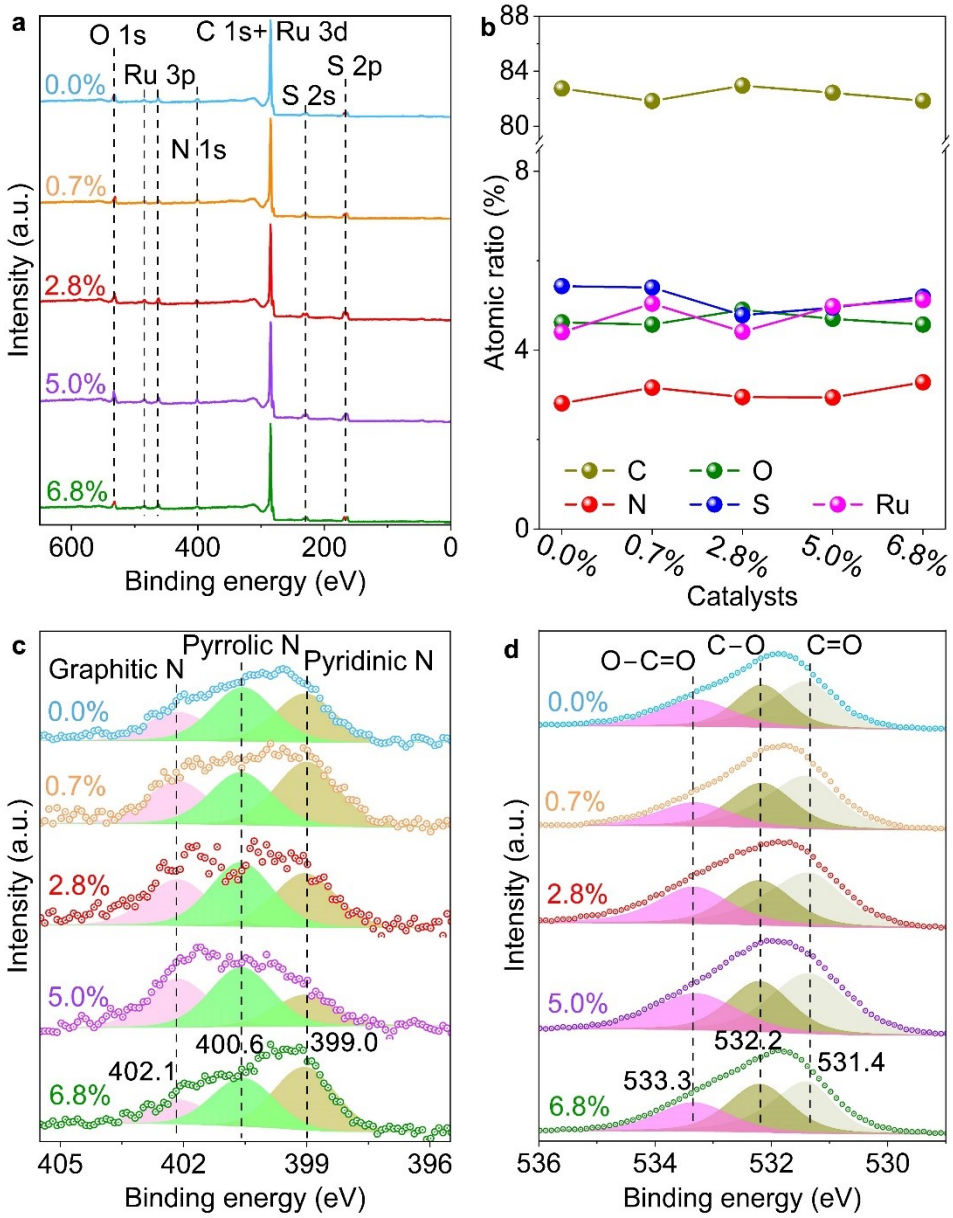

Fig. S10. XPS characterization of the s-RuS_2/NSG composites. (a) XPS survey spectra. (b) Comparison of the atomic ratios. High-resolution (c) N 1s and (d) O 1s XPS spectra.

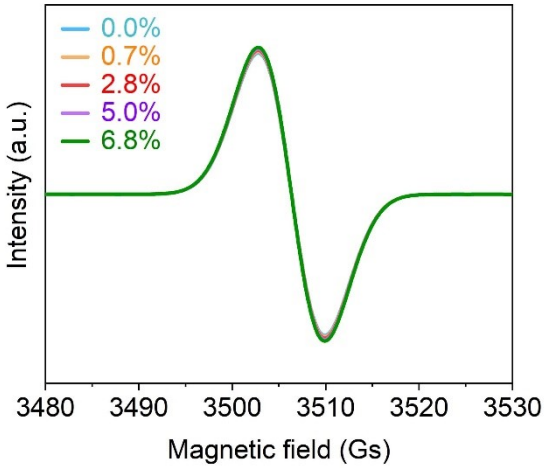

Fig. S11. Electron paramagnetic resonance (EPR) spectra of the s-RuS_2/NSG composites.

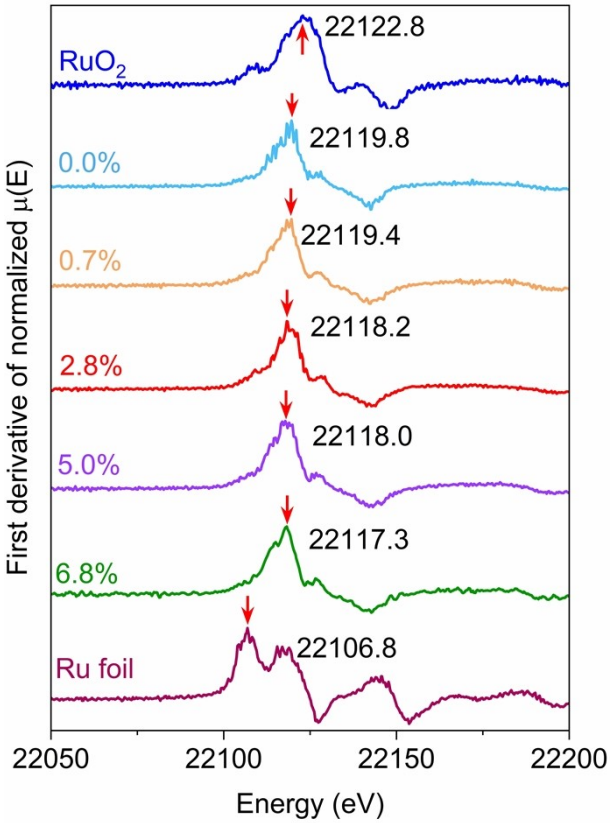

Fig. S12. First-derivative curves of Ru K-edge XANES spectra of s-RuS_2/NSG composites.

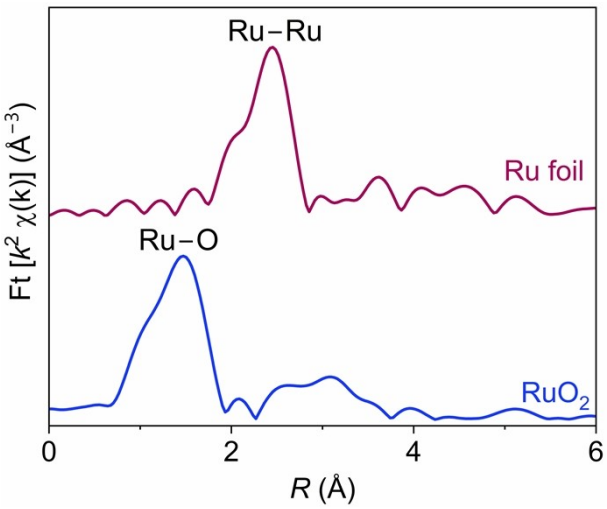

Fig. S13. Fourier-transformed Ru *K*-edge EXAFS spectra of RuO_2 and Ru foil.

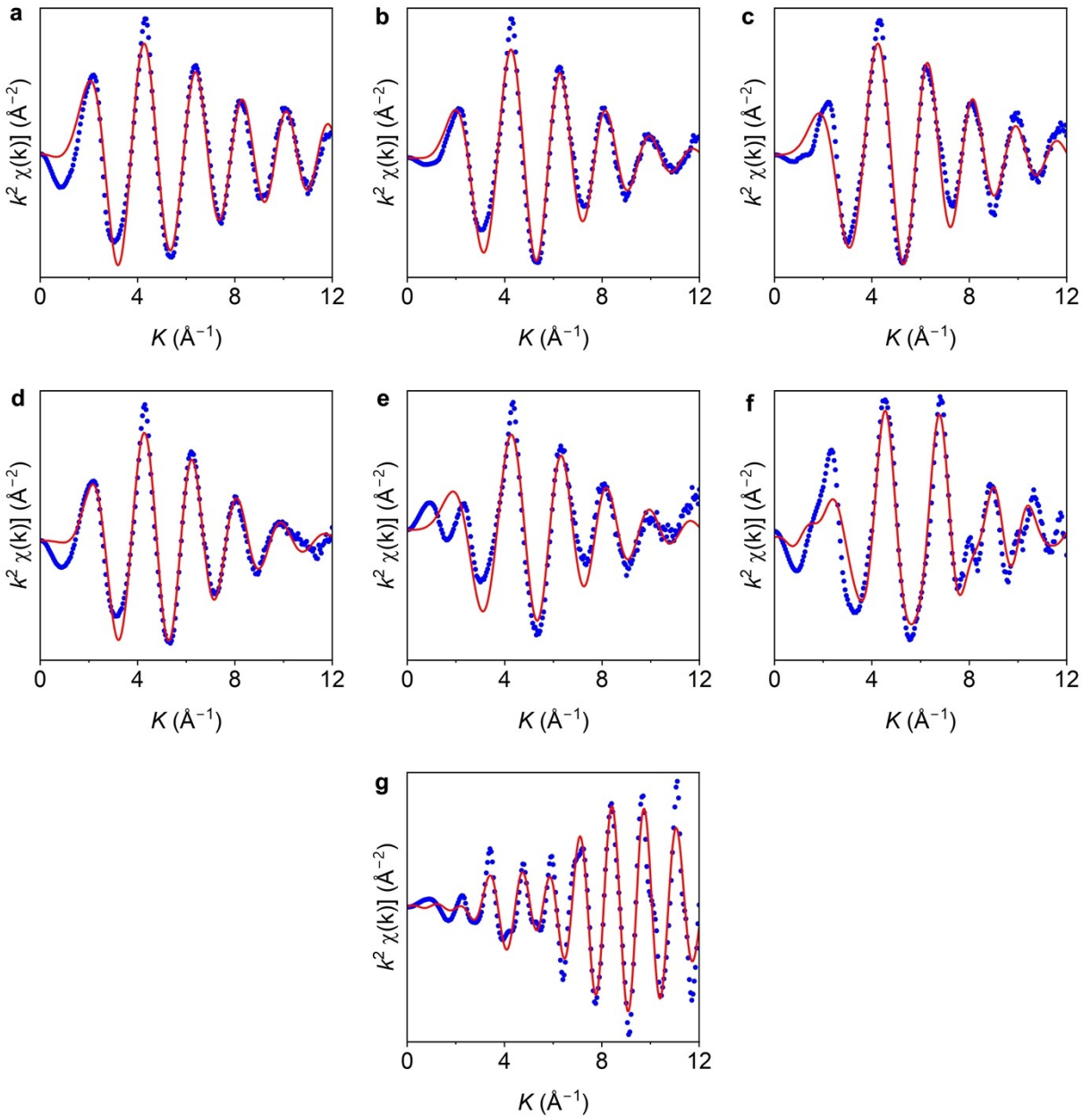

Fig. S14. EXAFS fitting of (a) RuS_2/NSG-0.0%, (b) RuS_2/NSG-0.7%, (c) RuS_2/NSG-2.8%, (d) RuS_2/NSG-5.0%, (e) RuS_2/NSG-6.8%, (f) RuO_2, and (g) Ru foil. Experimental data are shown as blue dots, and the corresponding fits are shown as red solid lines.

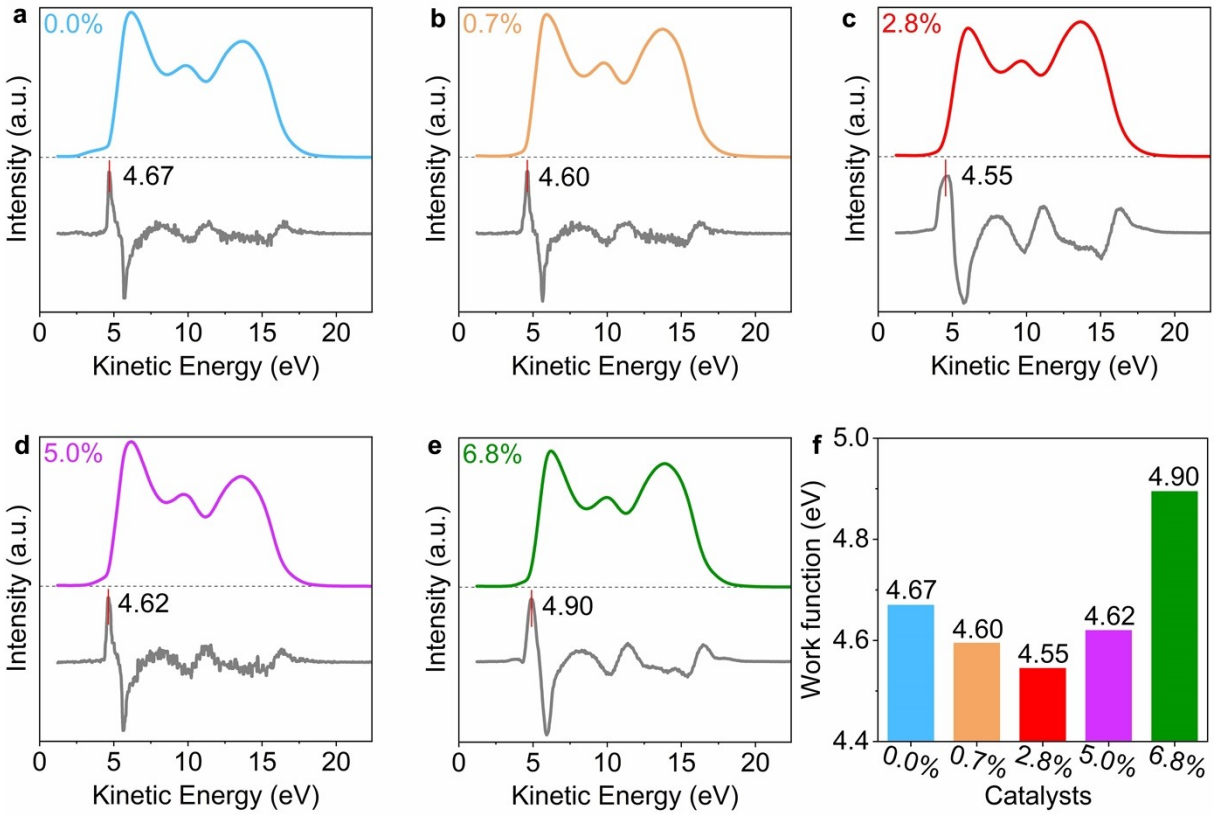

Fig. S15. UPS spectra and corresponding second derivative curve of (a) RuS_2/NSG-0.0%, (b) RuS_2/NSG-0.7%, (c) RuS_2/NSG-2.8%, (d) RuS_2/NSG-5.0%, and (e) RuS_2/NSG-6.8%. (f) UPS-derived work function.

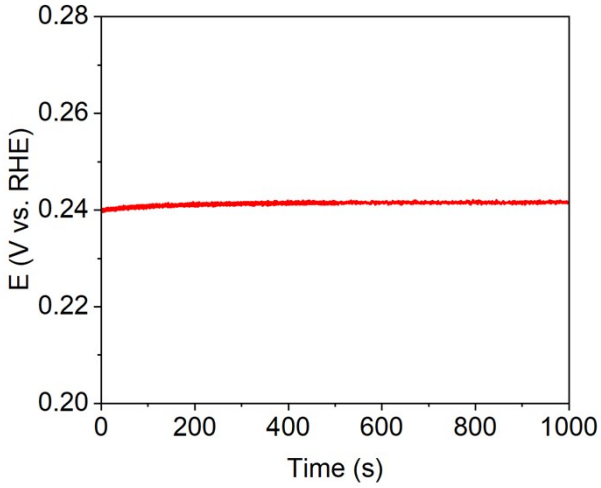

Fig. S16. The electrode potential of the saturated calomel electrode (SCE) measured against a commercial standard hydrogen electrode (SHE). Based on data collected over the time range 600-1000 s, the average electrode potential of our SCE was determined to be 0.242 V.

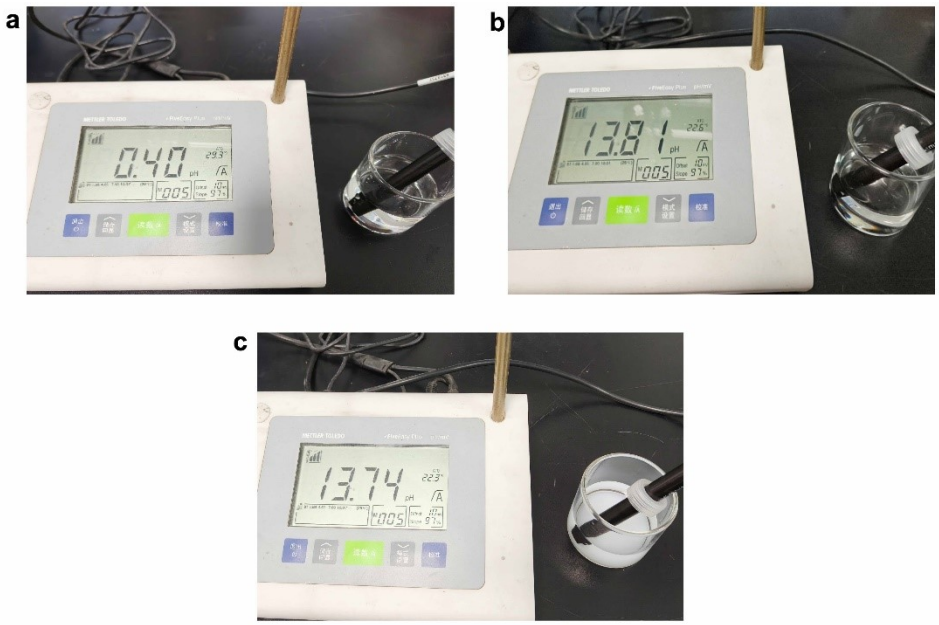

Fig. S17. Measuring the pH of electrolytes. (a) 0.5 M H_2SO_4 in deionized water, (b) 1.0 M KOH in deionized water, and (c) 1.0 M KOH in seawater.

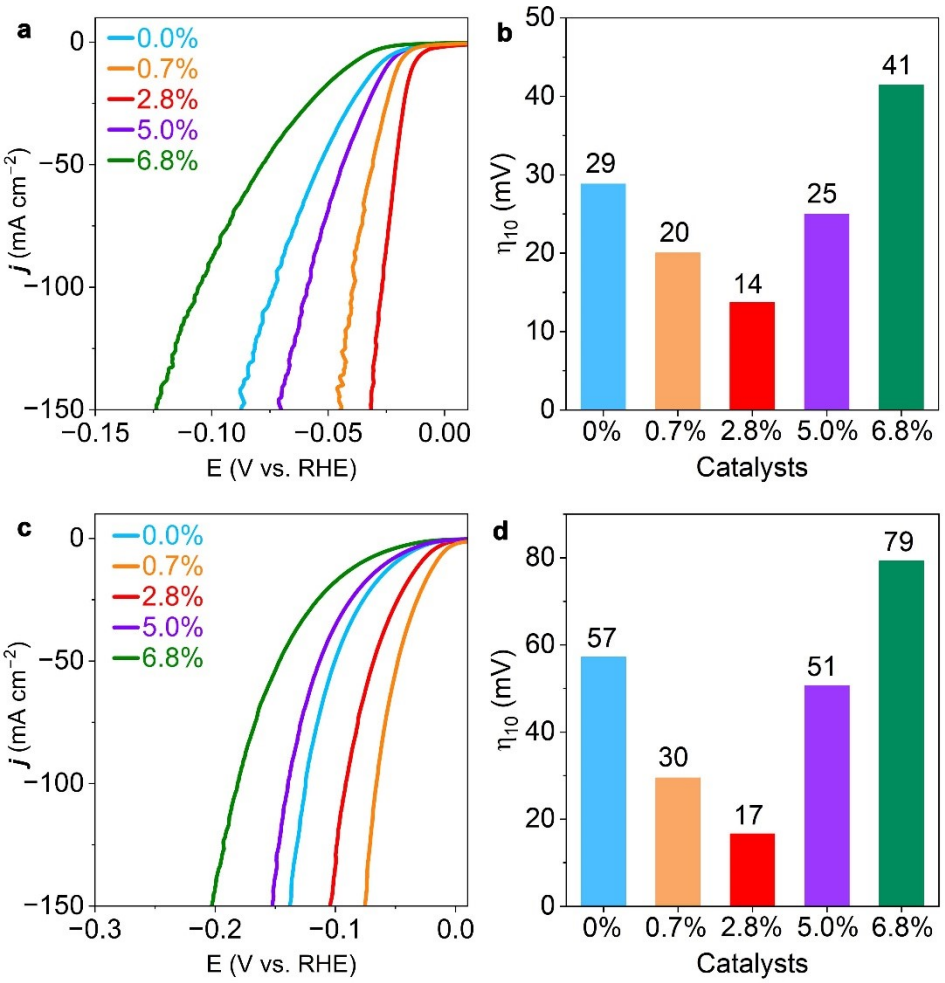

Fig. S18. (a) Polarization curves and (b) comparison of η_{10} for s-RuS_2/NSG in 0.5 M H_2SO_4 electrolyte. (c) Polarization curves and (d) comparison of η_{10} for s-RuS_2/NSG in 1.0 M KOH electrolyte.

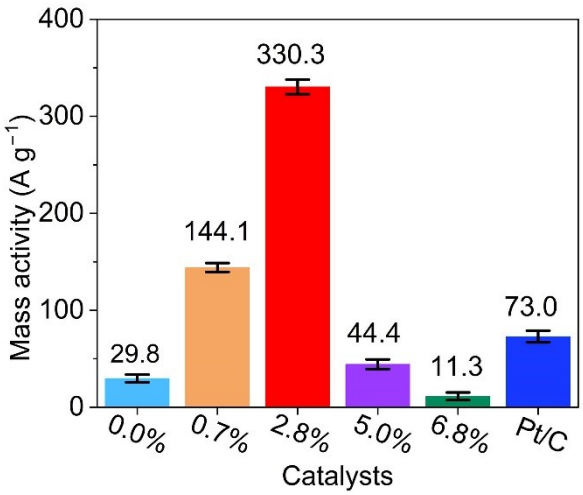

Fig. S19. Ru mass activity of s-RuS_2/NSG composites in comparison with the Pt mass activity of Pt/C.

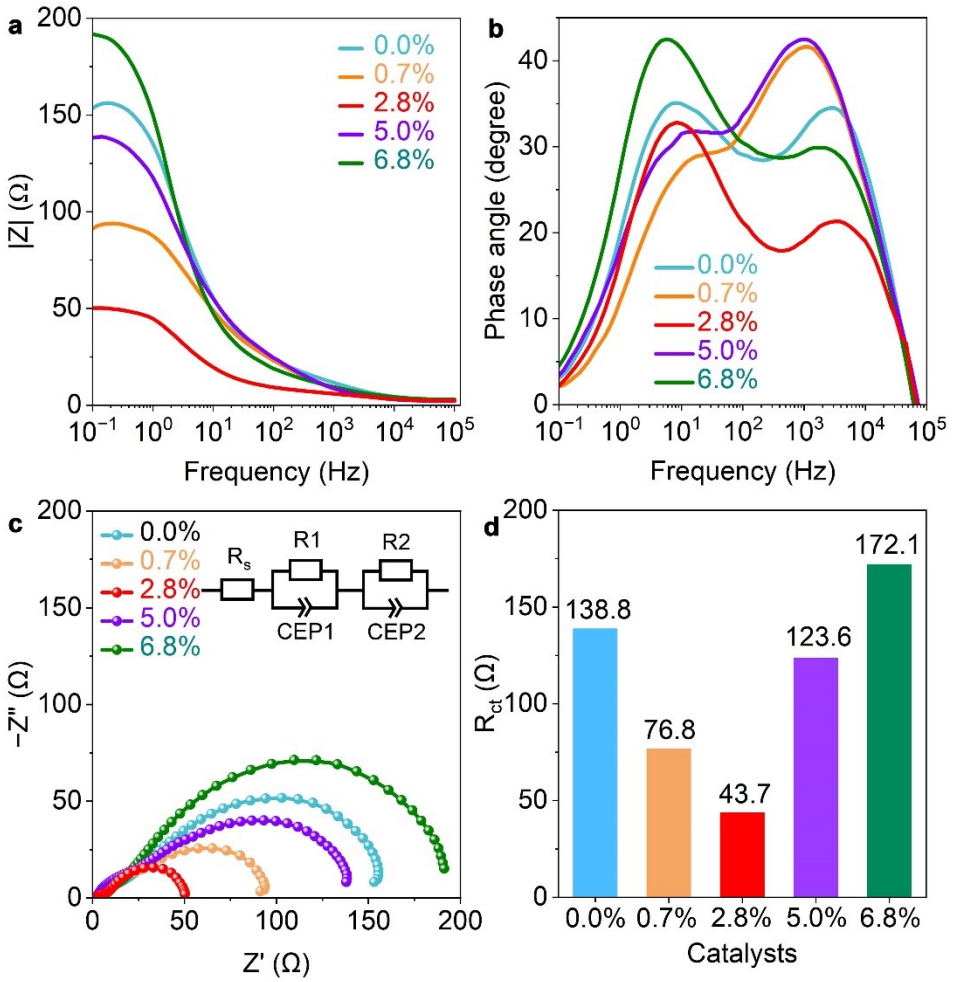

Fig. S20. (a) Bode magnitude plots (|Z| vs frequency) and (b) Bode phase plots of s-RuS_2/NSG. (c) Nyquist plots and (d) fitted R_{ct} of s-RuS_2/NSG.

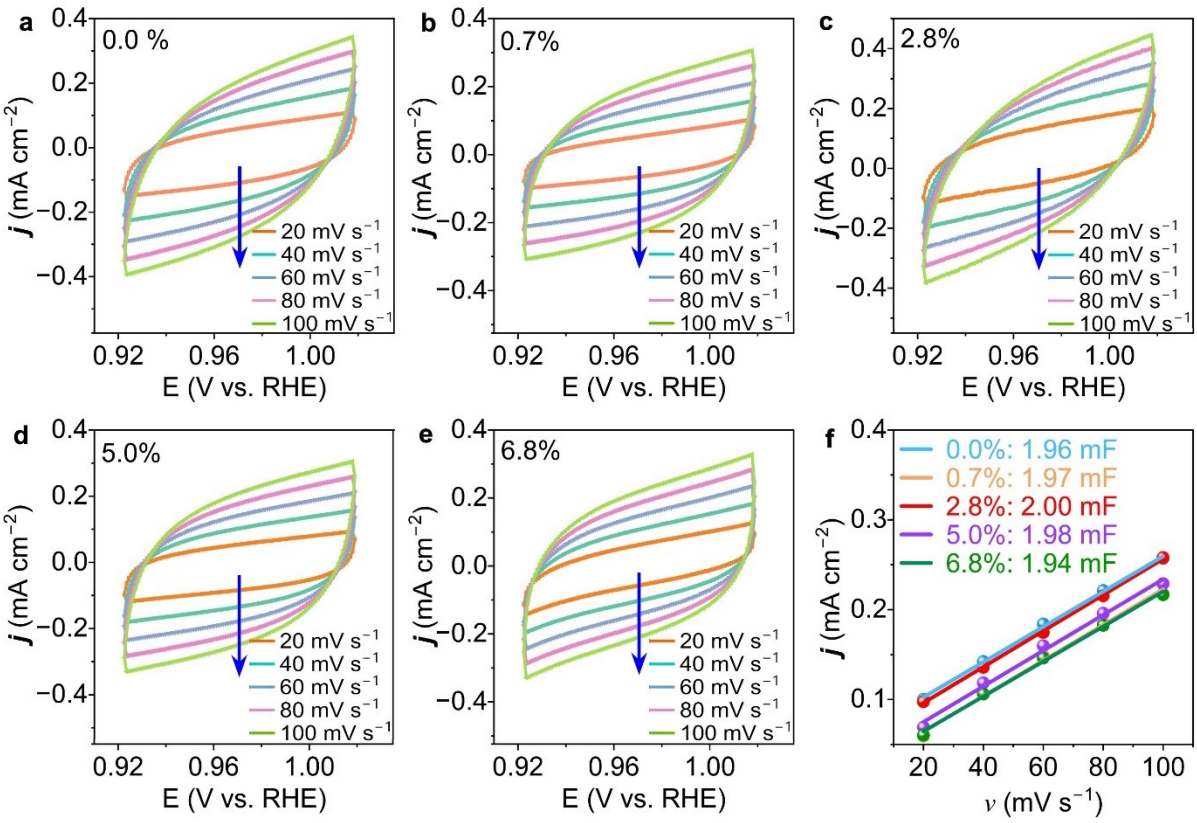

Fig. S21. CV curves of (a) RuS_2/NSG-0.0%, (b) RuS_2/NSG-0.7%, (c) RuS_2/NSG-2.8%, (d) RuS_2/NSG-5.0%, and (e) RuS_2/NSG-6.8% recorded at scan rates of 20, 40, 60, 80, and 100 mV s^{-1}. (f) The double-layer current density (j) as a function of the scan rate (v) for s-RuS_2/NSG composites, where the j is equal to 0.5 × (j_{anode} - $j_{cathode}$) acquired at 0.977 V.

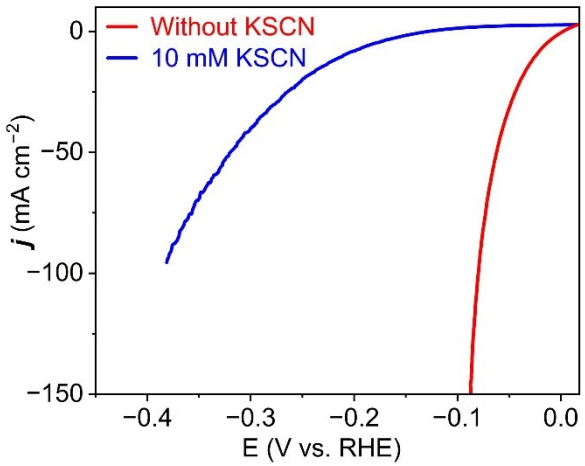

Fig. S22. KSCN poisoning experiment of RuS_2/NSG-2.8%. The drastic decrease in HER activity with 10 mM KSCN addition suggests that Ru is the active site.

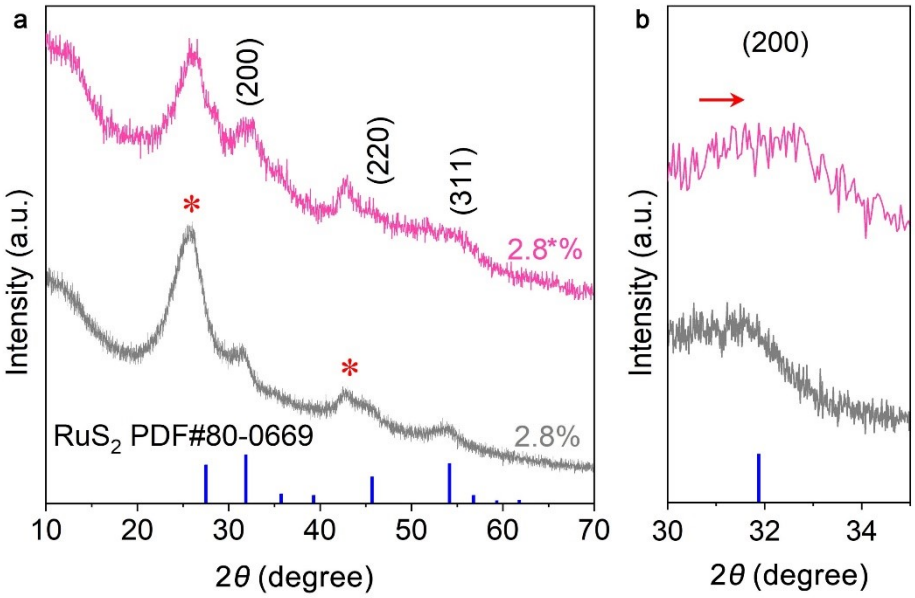

Fig. S23. XRD patterns of RuS_2/NSG-2.8*% compared with RuS_2/NSG-2.8%.

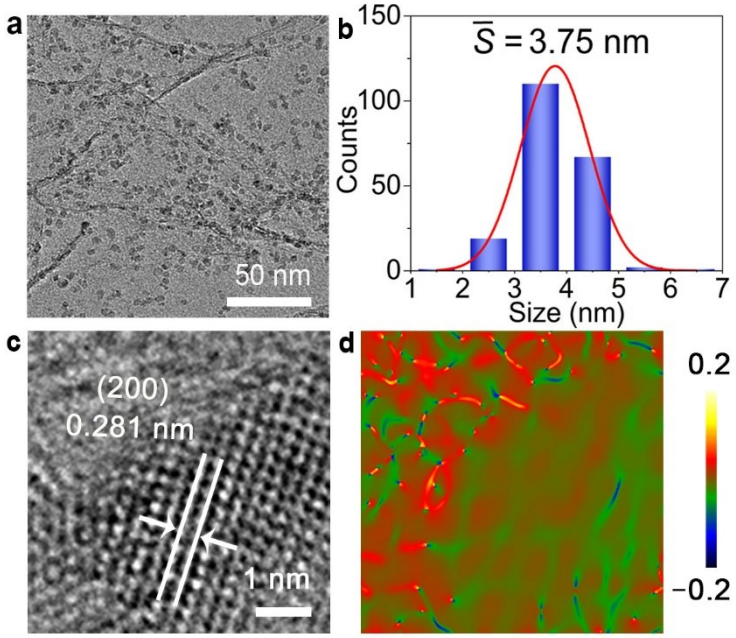

Fig. S24. (a) TEM, (b) particle size distribution, (c) HRTEM, and (d) GPA images of RuS_2/NSG-2.8*%.

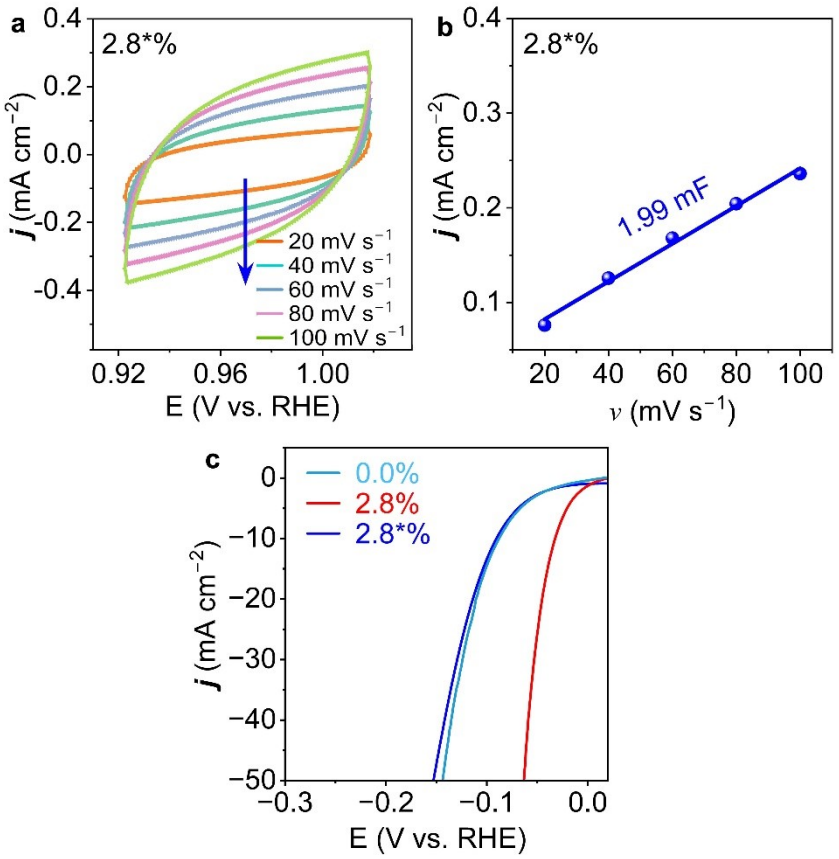

Fig. S25. (a) CV curves and (b) C_{dl} of RuS_2/NSG-2.8*%. (c) Comparison of the polarization curves of RuS_2/NSG-0.0%, RuS_2/NSG-2.8%, and RuS_2/NSG-2.8*%.

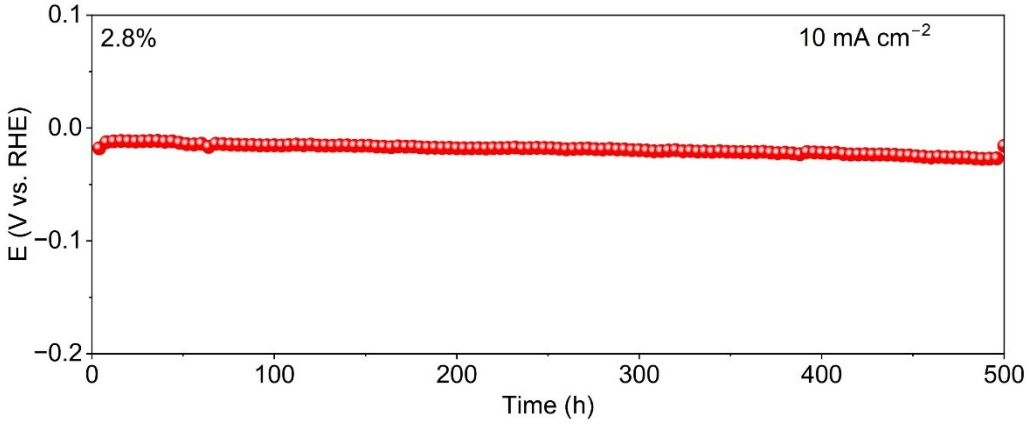

Fig. S26. Chronopotentiometry curve of RuS_2/NSG-2.8% recorded at 10 mA cm^{-2}.

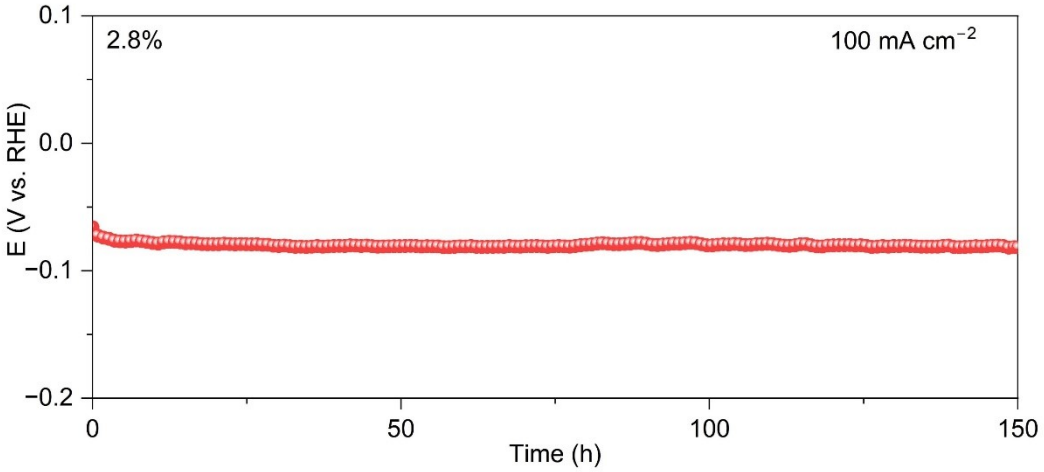

Fig. S27. Chronopotentiometry curve of RuS_2/NSG-2.8% recorded at 100 mA cm^{-2}.

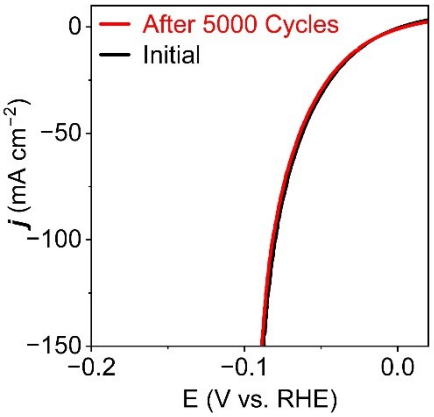

Fig. S28. Polarization curves of RuS_2/NSG-2.8% acquired before and after 5000 CV cycles.

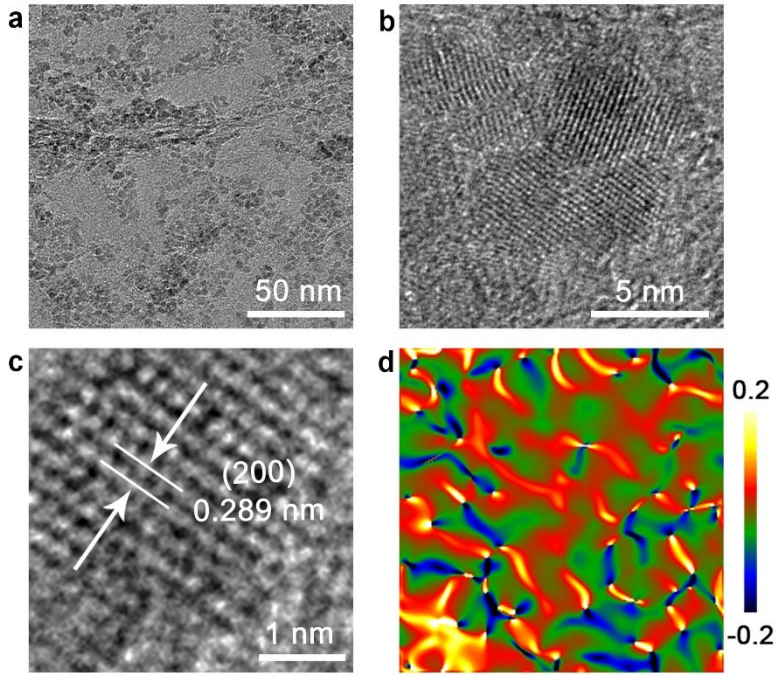

Fig. S29. (a) TEM, (b, c) HRTEM, and (d) GPA images of RuS_2/NSG-2.8% after 5000 CV cycles.

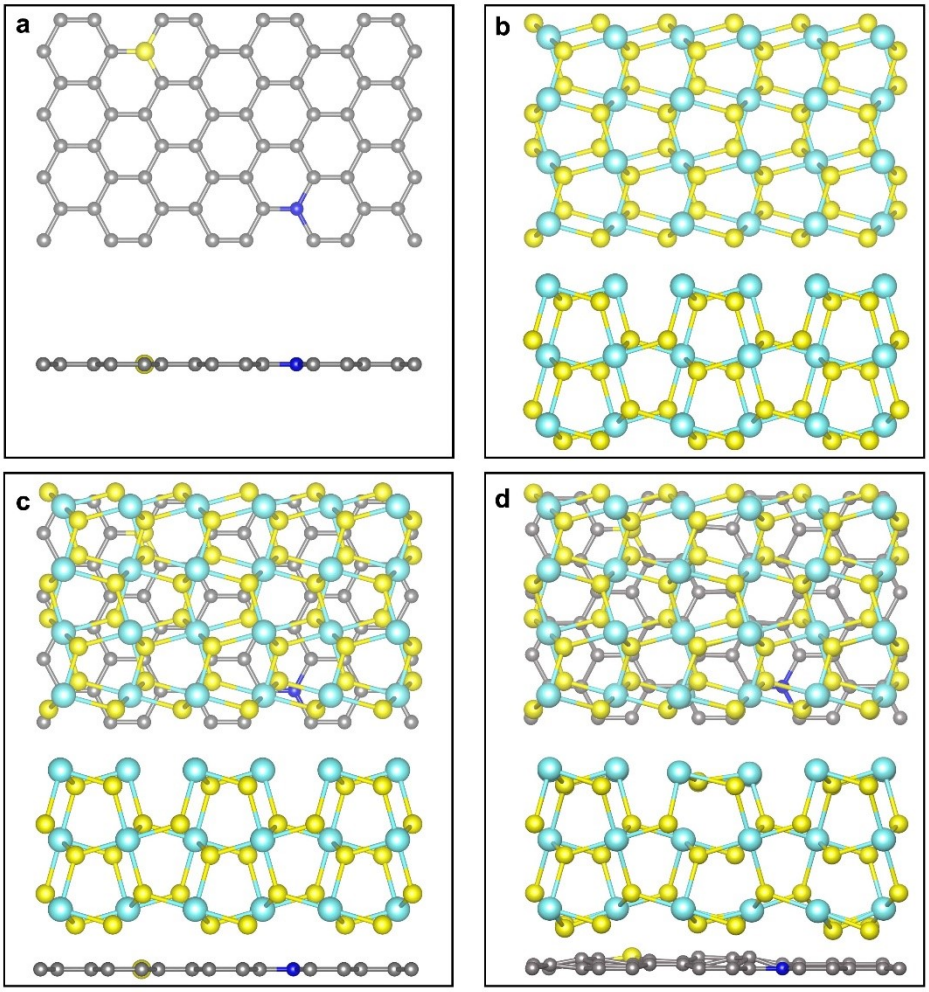

Fig. S30. (a) Top and side views of NSG containing one N and one S heteroatom. (b) Top and side views of RuS_2. (c) Top and side views of the RuS_2/NSG-0% heterostructure. (d) Top and side views of the RuS_2/NSG-0% structure after geometric relaxation. Unless otherwise stated, the yellow, blue, gray, and cyan spheres in the structural models represent sulfur, nitrogen, carbon, and ruthenium atoms, respectively.

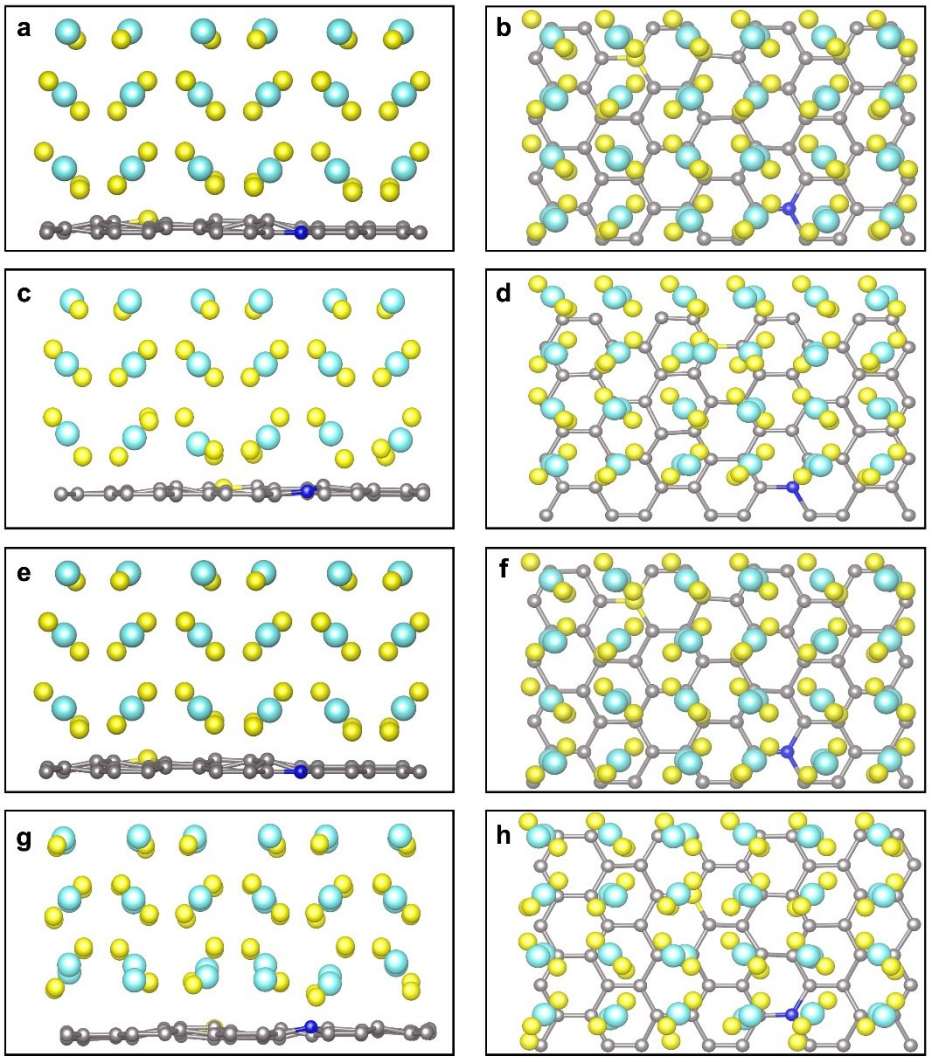

Fig. S31. Optimized structure models. Side and top views of (a, b) RuS_2/NSG-0.7%, (c, d) RuS_2/NSG-2.8%, (e, f) RuS_2/NSG-5.0%, and (g, h) RuS_2/NSG-6.8%.

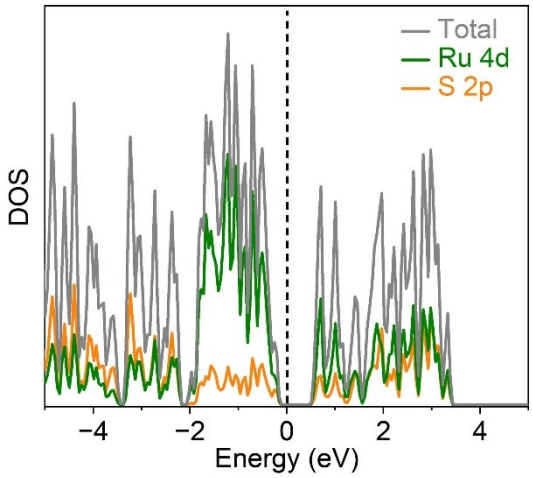

Fig. S32. The DOS of pristine RuS_2.

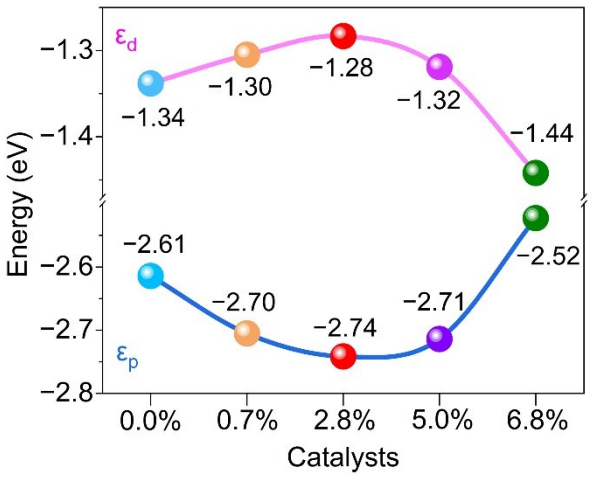

Fig. S33. The ε_d of Ru and ε_p of S in s-RuS_2/NSG composites as a function of the lattice strain in RuS_2.

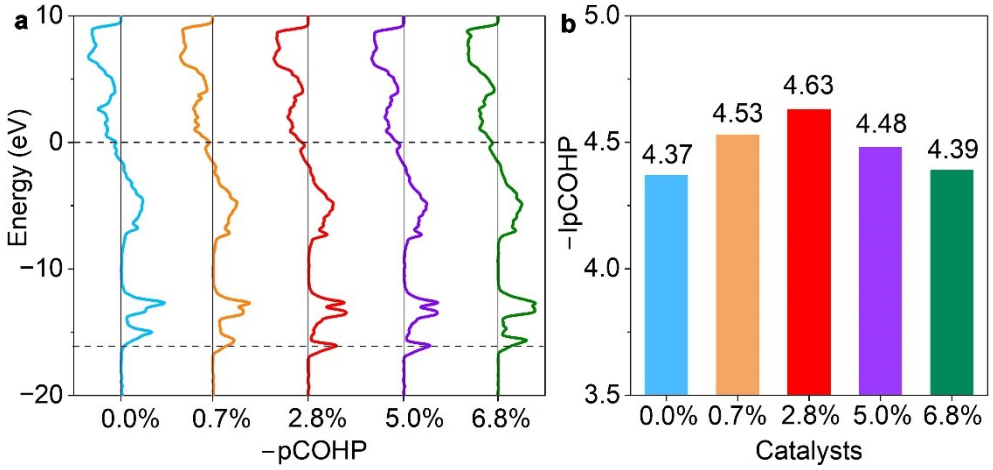

Fig. S34. (a) pCOHP and (b) IpCOHP of s-RuS_2/NSG.

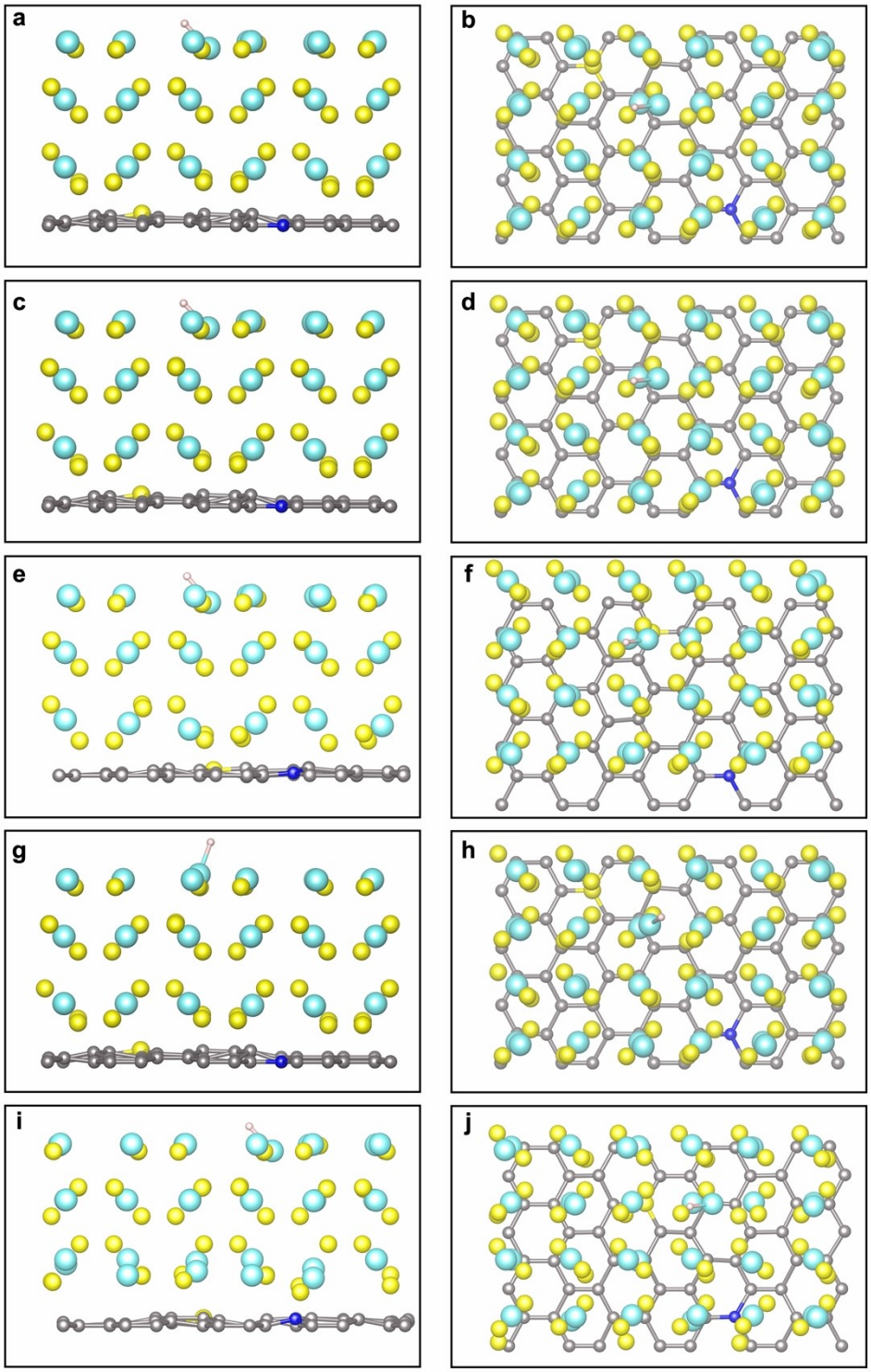

Fig. S35. Optimized configurations for *H adsorption. Side and top views of (a, b) RuS_2/NSG-0.0%, (c, d) RuS_2/NSG-0.7%, (e, f) RuS_2/NSG-2.8%, (g, H) RuS_2/NSG-5.0%, and (i, j) RuS_2/NSG-6.8%.

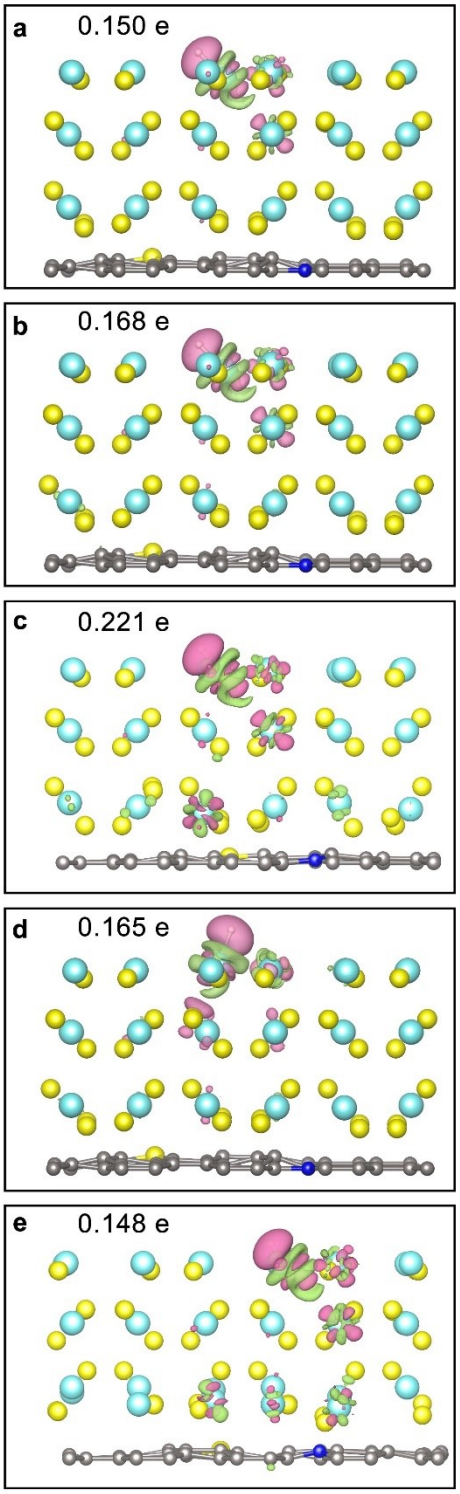

Fig. S36. CDD analyses of *H adsorption. Side views of (a) RuS_2/NSG-0.0%, (b) RuS_2/NSG-0.7%, (c) RuS_2/NSG-2.8%, (d) RuS_2/NSG-5.0%, and (e) RuS_2/NSG-6.8%. The pink and green regions represent the electron accumulation and depletion, respectively.

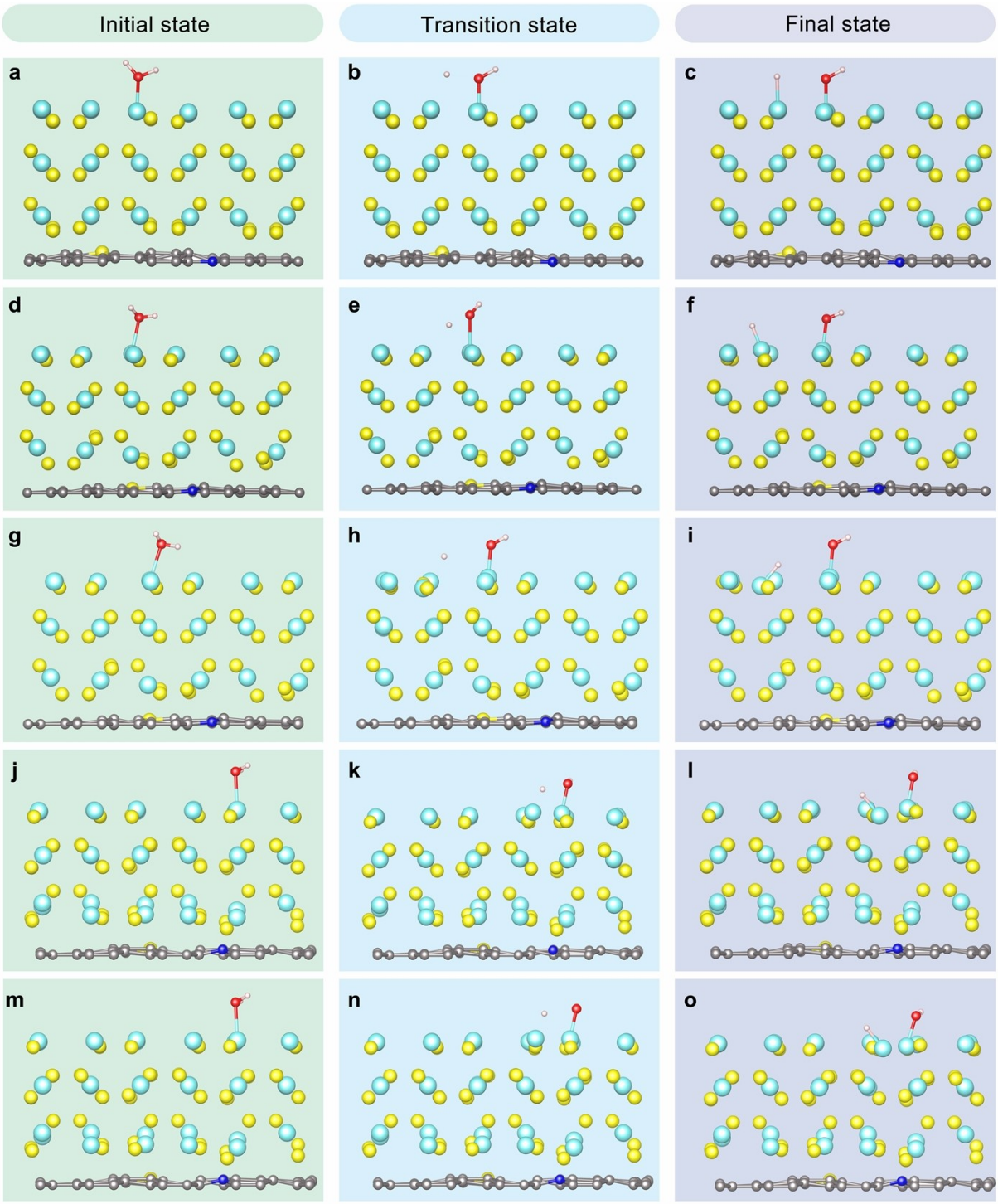

Fig. S37. The initial, transition, and final states of water adsorption and dissociation on (a-c) RuS_2/NSG-0.0%, (d-f) RuS_2/NSG-0.7%, (g-i) RuS_2/NSG-2.8%, (j-l) RuS_2/NSG-5.0%, and (m-o) RuS_2/NSG-6.8%.

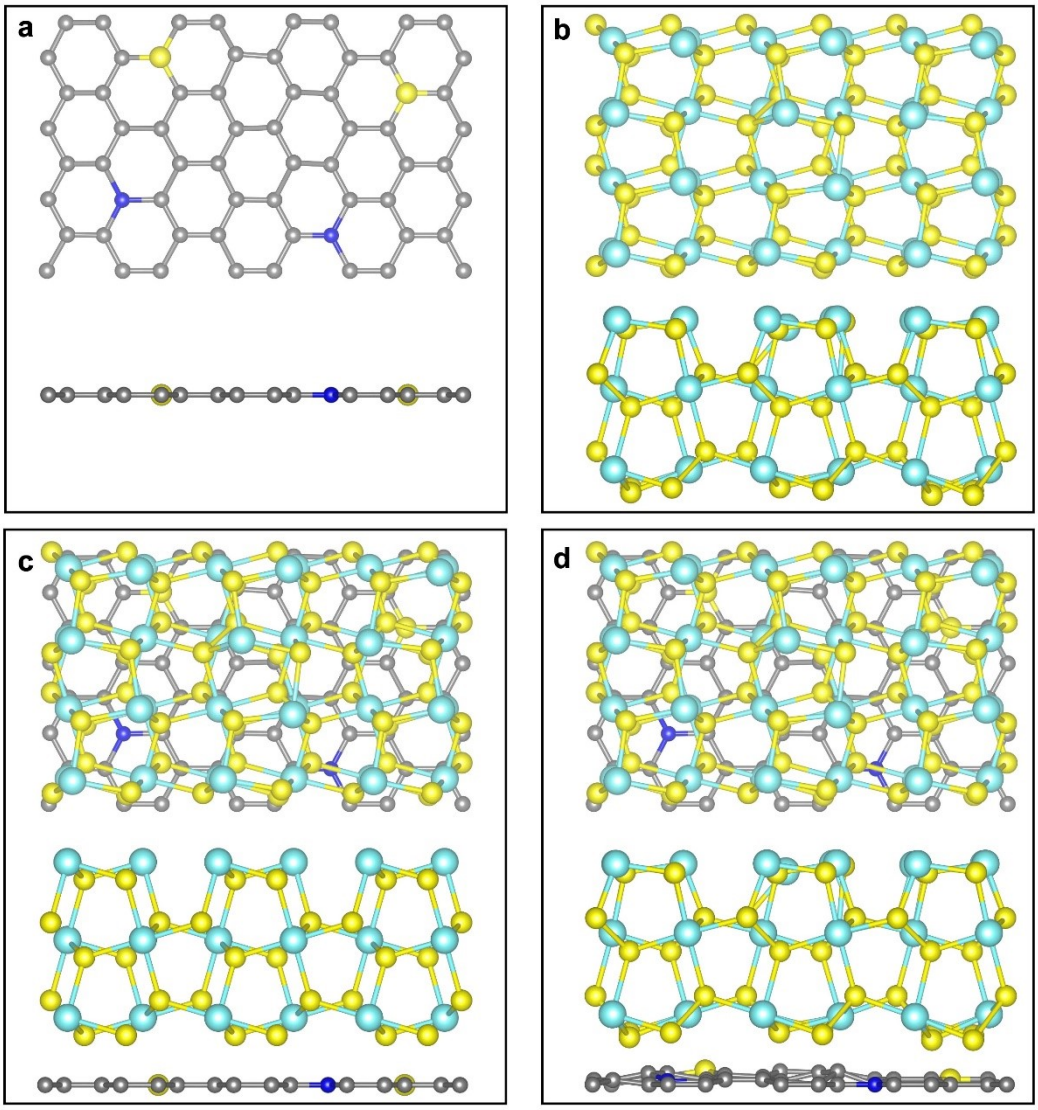

Fig. S38. (a) Top and side views of NSG containing two N and two S heteroatoms. (b) Top and side views of RuS_2. (c) Top and side views of the RuS_2/NSG-0% heterostructure with two N and two S heteroatoms. (d) Top and side views of the RuS_2/NSG-0% with two N and two S heteroatoms after structural optimization.

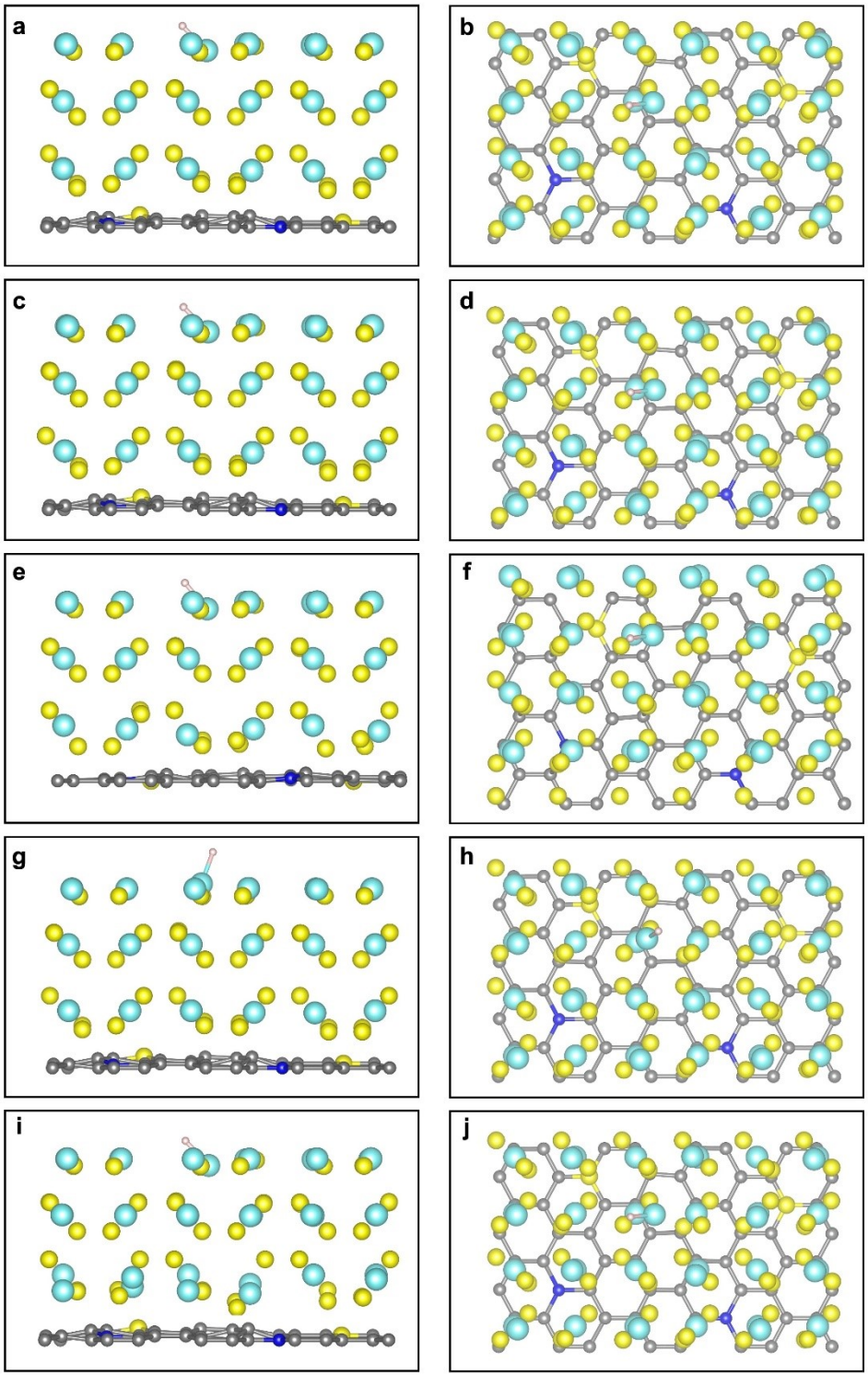

Fig. S39. Optimized configurations for *H adsorption on s-RuS_2/NSG with two N and two S heteroatoms. Side and top views of (a, b) RuS_2/NSG-0.0%, (c, d) RuS_2/NSG-0.7%, (e, f) RuS_2/NSG-2.8%, (g, H) RuS_2/NSG-5.0%, and (i, j) RuS_2/NSG-6.8%.

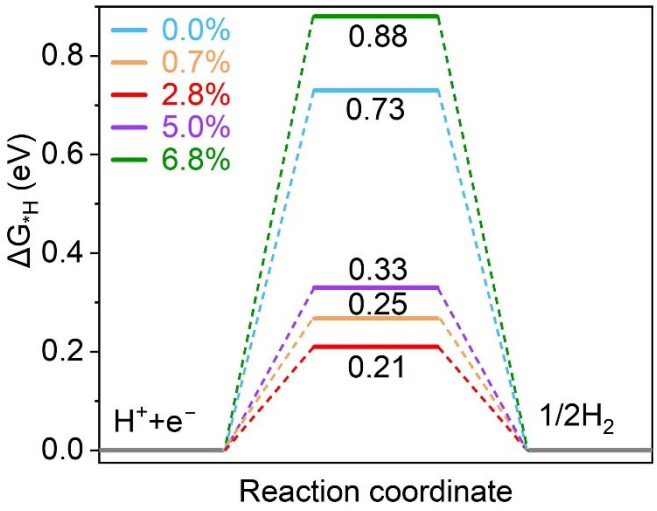

Fig. S40. Calculated ΔG_{*H} of s-RuS_2/NSG with two N and two S heteroatoms.

3 Supporting Tables

Table S1. Coefficients of thermal expansion (CTE) of graphene and TMSs.

Materials	CTE (K^{-1})	Reference
Graphene	-4.8×10^{-6}	*Phys. Rev. Lett.* 2009, 102, 046808.
FeS_2	9.25×10^{-6}	*Am. Mineral.* 1964, 49, 206
CoS_2	12.89×10^{-6}	*Am. Mineral.* 1964, 49, 206
NiS_2	11.4×10^{-6}	*Acta Chem. Scand.* 1969, 23, 2325
CuS	24.2×10^{-6}	*Inorg. Mater.* 2007, 43, 573
ZnS	6.7×10^{-6}	*Appl. Surf. Sci.* 1999, 151, 203
MoS_2	17.4×10^{-6}	*ACS Appl. Mater. Interfaces* 2020, 12, 45101
Ag_2S	20.0×10^{-6}	*Thermochim. Acta* 2018, 660, 1
CdS	6.5×10^{-6}	*Semicond. Sci. Technol.* 2000, 15, 408
SnS_2	9.4×10^{-6}	*Acta Mater.* 2015, 82, 212
PtS_2	40.0×10^{-6}	*Acta Chem. Scand.* 1959, 13, 1767
PbS	20.0×10^{-6}	*J. Phys. Chem. C* 2014, 118, 35, 20585
RuS_2	47.0×10^{-6}	*Chem. Rev.* 1985, 85, 1
Bi_2S_3	52.6×10^{-6}	*Phys. Scr.* 2023, 98, 125938

Table S2. Lattice fringes of the s-TMSs measured from the aberration-corrected HRTEM images in Fig. 2.

Materials	Crystal facet	Lattice spacing (nm) (Theoretical)	Lattice spacing (nm) (Experimental)	Strain
VS/NSG	(102)	0.205	0.219	6.8%
Cr_5S_6/NSG	(110)	0.298	0.303	1.7%
MnS/NSG	(200)	0.261	0.291	11.5%
FeS_2/NSG	(111)	0.313	0.341	8.9%
CoS_2/NSG	(200)	0.277	0.291	5.1%
NiS_2/NSG	(222)	0.163	0.169	3.7%
CuS/NSG	(103)	0.281	0.289	2.8%
ZnS/NSG	(111)	0.312	0.329	5.4%
MoS_2/NSG	(101)	0.267	0.271	1.5%
RuS_2/NSG	(200)	0.281	0.289	2.8%
Rh_2S_3/NSG	(211)	0.301	0.320	6.3%
PdS/NSG	(211)	0.264	0.275	4.2%
Ag_2S/NSG	(-103)	0.238	0.246	3.4%
CdS/NSG	(110)	0.206	0.213	3.4%
$In_{2.77}S_4$/NSG	(222)	0.310	0.318	2.6%
SnS_2/NSG	(100)	0.316	0.338	7.0%
ReS_2/NSG	（004）	0.303	0.329	8.6%
OsS_2/NSG	(200)	0.281	0.291	3.6%
PtS/NSG	(102)	0.230	0.239	4.3%
PbS/NSG	(200)	0.297	0.307	3.9%
Bi_2S_3/NSG	(301)	0.272	0.278	2.2%

Table S3. XAFS fitting parameters for s-RuS_2/NSG composites, Ru foil, and RuO_2.

Samples	Shell	*CN*[a]	*R* (Å)[b]	σ^2 (Å$^2\cdot10^{-3}$)[c]	ΔE_0 (eV)[d]	R factor (%)
Ru foil	Ru-Ru	12*	2.66 ± 0.02	0.0041	5.31 ± 1.82	1.1
	Ru-O	6*	1.95 ± 0.02	0.0027	1.40 ± 1.93	
RuO_2	Ru-O-Ru1	2*	3.06 ± 0.02	0.0065	6.11 ± 1.15	1.6
	Ru-O-Ru2	8*	3.43 ± 0.04	0.0032	2.74 ± 1.97	
RuS_2/NSG-0.0%	Ru-S	6.1 ± 0.5	2.06 ± 0.03	0.0021	1.19 ± 3.01	1.5
RuS_2/NSG-0.7%	Ru-S	6.0 ± 0.3	2.12 ± 0.02	0.0038	2.78 ± 2.25	0.4
RuS_2/NSG-2.8%	Ru-S	5.7 ± 0.4	2.23 ± 0.01	0.0083	2.37 ± 2.15	0.6
RuS_2/NSG-5.0%	Ru-S	5.5 ± 0.3	2.27 ± 0.05	0.0097	6.28 ± 3.63	0.9
RuS_2/NSG-6.8%	Ru-S	5.1 ± 0.2	2.29 ± 0.02	0.0095	5.04 ± 2.62	1.5

[a] *CN*: coordination number; [b] *R*: distance between absorber and backscatter atoms; [c] σ^2: Debye-Waller factor to account for both thermal and structural disorders; [d] ΔE_0: inner potential correction; *R* factor indicates the goodness of the fit. The amplitude reduction factor (S_0^2) was fixed to 0.90, according to the experimental EXAFS fit of Ru foil by constraining the CN as the known crystallographic value. Fitting range: $3.0 \le k$ (Å^{-1}) ≤ 12.0 and $1.5 \le R$ (Å) $\le$ ~3.2 for Ru foil; $3.0 \le k$ (Å^{-1}) ≤ 12.0 and $1.0 \le R$ (Å) $\le$ ~2.5 for s-RuS_2/NSG composite. Reasonable parameter ranges for EXAFS fitting are generally as follows: $0.700 < S_0^2 < 1.0$; $CN > 0$; $\sigma^2 > 0$ Å^2; $\Delta E_0 < 10$ eV; *R* factor < 0.02.

Table S4. Catalytic performance comparison of RuS_2/NSG-2.8% with previously reported Ru-based HER electrocatalysts in alkaline seawater.

Catalysts	η_{10} (mV)	Tafel slope (mV dec^{-1})	Reference
$MoSe_2$-$RuSe_2$/NF	50	/	*J. Mater. Chem. A*, 2026,14, 8989
$Ni_{20}V$	110	/	*Adv. Funct. Mater.,* 2026, 36, e16387
V-Ru/KB	30	/	*Adv. Funct. Mater.,* 2026, 36, e12343
Ru/$Ti_3C_2O_x$@NF	33	41.5	*Nano Energy,* 2026, 147, 111582
FeRu/MoO_2@Mo	65	/	*Small,* 2026, 22, 2412729
RuMo/Cu_2O@C	24	49.9	*Adv. Mater.,* 2025, 37, 2416658
Ru/CeO_2-Ov-2	41	/	*J. Energy Chem.,* 2025, 102, 618
Ru/$RuSe_x$	26	36	*Appl. Catal. B,* 2025, 379, 125720
$NiSe_2$-$RuSe_2$/NF	26	46.7	*Chem. Eng. J.,* 2025, 512, 162567
FeCoNiMnRu HEA	35	41	*Chem. Eng. J.,* 2025, 509, 161070
N-NiHf@NF	68	198	*J. Mater. Chem. A,* 2025, 13, 28026
Ru/CeO_2-H_2O_2	47	39	*Inorg. Chem. Front.,* 2025,12, 821
HELH/HEMS-6h	71	45.3	*Langmuir 2025, 41, 28, 18872*
NiMoP	50.3	49.7	*Sustain. Energy Fuels,* 2025, 9, 6811
Fe-CoP_x/NF	32	48.2	*ACS Sustainable Chem. Eng.,* 2025, 13, 1118
Ni/$Co(OH)_2$-Ru@NF	33	/	*Small,* 2025, 21, 2410086
$NiMoO_4$/Ni/B-CNTs	48	42	*Energy Fuels,* 2025, 39, 19388
CoP–MXene	101	45	*ACS Appl. Mater. Interfaces,* 2025, 17, 52212
Ru-BO_x-OH-300	22	16.9	*Energy Environ. Sci.*, 2024,17, 3888
Mox-$Ni_{0.85}Se$/$MoSe_2$	110	70.12	*Chem. Sci.,* 2024,15, 1123-1131
RuMo-NPCSPC	85	/	*J. Colloid Interface Sci.,* 2025, 699, 138213
Ru-Co_2P/NPC-2	26.0	41.5	*Small,* 2024, 21, 2406900
Ru/SNC	30	41.5	*EES Catal.,* 2024, 2, 932
Cu-Ru/WC@C	24	28	*Appl. Catal. B,* 2024, 357, 124330
$Co_3(PO_4)_2$@MXene	58.6	43.8	*Inorg. Chem. Front.,* 2024,11, 6909
Co_2P/$CoMoP_2$	43	58	*Inorg. Chem. Front.,* 2024,11, 1978
Ru/NC	46	38	*Renew. Energy,* 2024, 227, 120468
RhCoNi-MOF	50	73	*ACS Sustainable Chem. Eng.* 2024, 12, 1038
Act-Co-NiPx	97	/	*Chem. Eng. J.,* 2024, 499, 155925
Pt-CoS/$Co(OH)_2$/C	87	/	*Rare Met.,* 2024, 43, 511
Ru/WO_3-O_V	38	35.6	*J. Colloid Interface Sci.,* 2024, 660, 321
BPed-Ru-GR	51	50	*Adv. Energy Mater.,* 2023, 13, 2302727
Ru–$Ni_{0.85}Se$/CC	44.2	107.35	*Energy Fuels,* 2023, 37, 18*204*
RuSb	39	30	*Appl. Catal. B,* 2023, 333, 122771
NC@CrN/Ni	28	/	*J. Colloid Interface Sci.,* 2023, 646, 361
$Ru_{22}NiMoP_2$/NF	52	42	*Sustain. Energy Fuels,* 2023,7, 4677
Co@RuCo-3	51	30	*Appl. Catal. B,* 2022, 315, 121554
RuS_2/NSG-2.8%	**24**	**24**	**This work**